

# Determination of Hydrogen and Deuterium Inventory of Pre-Treated Targets Using Laser-Induced Desorption

Charlie Spork  
Faculty of Geosciences,  
University of Utrecht,  
Utrecht, The Netherlands

Supervisors:  
dr. Hennie van der Meiden  
dr. Pedro Zeijlmans van Emmichoven

January 2013

## Abstract

Laser-Induced Desorption-Quadrupole Mass Spectrometry (LID-QMS) is a diagnostic method in which a quadrupole mass analyzer is used to measure the amount of material that is desorbed from a sample by firing a spot laser on the surface. An LID-QMS system has been set up at the Target Exchange and Analysis Chamber (TEAC) of the plasma generator Magnum-PSI in order to investigate the first principles of laser-induced desorption of hydrogen isotopes from plasma facing component (PFC) materials. Two LID-QMS experiments with pre-treated targets were conducted in which the local hydrogen and deuterium concentration of the samples was determined. The most important uncertainty in the observed concentrations resulted from the determination of the desorbed area  $A_d$ . This area is essential for obtaining the D and H concentrations of the targets but is difficult to determine. Furthermore, a first attempt to perform an absolute calibration of the LID-QMS system at the TEAC was unsuccessful. Fulfilment of this absolute calibration is a priority for further research. The experimental work was supported by theoretical modeling in TMAP7. TMAP7 analysis showed that, for a single 3.0 ms laser pulse on a tungsten (W) surface, desorption percentages are higher than 90% for maximum surface temperatures  $T_{max} \geq 1300$  K.

# Contents

<b>1</b>	<b>Introduction</b>	<b>4</b>
<b>2</b>	<b>Theory</b>	<b>7</b>
2.1	Laser heating of surface . . . . .	7
2.2	The desorbed area . . . . .	8
2.3	Balmer line emissions . . . . .	9
<b>3</b>	<b>Analysis: TMAP7</b>	<b>11</b>
3.1	Modeling LID on tungsten surfaces . . . . .	11
3.2	Thermal boundary conditions . . . . .	12
3.3	Mobile and trapped deuterium . . . . .	13
<b>4</b>	<b>Experimental Methods</b>	<b>14</b>
4.1	Overview LID-QMS in TEAC . . . . .	14
4.2	QMS analysis . . . . .	15
4.2.1	Absolute sensitivity calibration of QMS . . . . .	15
4.3	Experimental procedure LID-QMS . . . . .	17
4.4	LID-QMS experiments . . . . .	19
4.4.1	EFDA targets . . . . .	19
4.4.2	Plasma-exposed targets . . . . .	20
<b>5</b>	<b>Results</b>	<b>23</b>
5.1	TMAP7 . . . . .	23
5.2	EFDA targets . . . . .	27
5.2.1	D and H concentrations . . . . .	27
5.2.2	Uncertainties in D and H concentrations . . . . .	28
5.2.3	Multiple LID shots . . . . .	29
5.2.4	Laser output energy $E_L$ . . . . .	30
5.2.5	Optical microscopy . . . . .	31
5.3	Plasma-exposed targets . . . . .	33
5.3.1	Uncertainties in D and H concentrations . . . . .	33
5.3.2	Radial D concentration profile . . . . .	34
5.3.3	TDS . . . . .	35
5.3.4	Optical microscopy . . . . .	36
<b>6</b>	<b>Discussion</b>	<b>37</b>
6.1	Physical background of TMAP7 results . . . . .	37
6.2	Determination of desorbed area $A_d$ . . . . .	38
6.3	Comparison TMAP7 and experiment . . . . .	39
<b>7</b>	<b>Conclusion</b>	<b>40</b>
7.1	Recommendations for further research . . . . .	41
<b>A</b>	<b>TMAP7: Trapped D Profile</b>	<b>43</b>
<b>B</b>	<b>TMAP7: Mobile D Profile</b>	<b>44</b>

## Acknowledgements

First of all, I wish to express my gratitude to my supervisors, Hennie van der Meiden and Pedro Zeijlmans van Emmichoven, for their support and for the fruitful collaboration of the past few months. Special thanks go to Rianne 't Hoen, for her advice and especially, for her help regarding the experiments with the plasma-exposed targets. I am further indebted to John Scholten for supervising both LID-QMS experiments at the TEAC. I would also like to acknowledge my fellow students at DIFFER who have made my time there an enjoyable one.

Last but not least, I wish to thank my family and friends for their everlasting support. In particular, I would like to thank Calvin Broadus, Shawn Carter and Jonathan Smith for being there for me and sharing their experiences.

# 1 Introduction

A major step in the world's tokamak fusion program will be the development of the International Thermonuclear Experimental Reactor (ITER). Future power generation in ITER will be based on the fusion of two hydrogen isotopes [1]: deuterium (D) and tritium (T). In order to achieve sufficient fusion reactions, a D-T plasma with a temperature in the range of 100 to 200 million °C will be maintained inside the reactor [1]. In the D-T fusion reaction a helium nucleus<sup>1</sup> and a high-energy neutron are formed [1]:



Deuterium is a stable hydrogen isotope and is widely available as it can be extracted from ordinary seawater [1].<sup>2</sup> Tritium - on the other hand - is a *radioactive* isotope of hydrogen with a half-life of 12.3 years [1].<sup>3</sup> Tritium is not abundant in nature and therefore tritium will have to be produced on-site. For this purpose, a lithium blanket will be constructed around the burn chamber [1]. The energetic neutrons that are created in the D-T plasma react with the lithium in the blanket to produce tritium [1], according to:



Tritium is therefore an intermediate product in the fusion reactor process. Nonetheless, it is anticipated that unburned tritium -and similarly deuterium- will be deposited on the surfaces and in the bulk of the plasma facing components (PFCs) of ITER [2–5].

A cross-sectional view of ITER is depicted in Fig. 1, showing the current design choice of PFCs in ITER. In the current design a beryllium-clad covers the first wall of the vacuum vessel, the upper baffle and the dome of the divertor are composed of tungsten (W) and the remaining high power divertor regions will consist of carbon fibre composites, although a change to a full W divertor is now considered for the D-T operation phase [2]. With such choices of PFCs in ITER, tritium retention is predominantly caused by co-deposition of tritium with carbon and beryllium [2]. Another, but smaller, contribution is expected to come from tritium settling in the bulk of the W divertor tiles [2]. For safety reasons, the total tritium inventory within the reactor vessel is not allowed to exceed 700 g-T [3]. When this administrative limit is reached, ITER operation will temporarily have to be ceased and the reactor vessel will have to be cleaned in order to reduce the tritium inventory to an acceptable level. The total tritium inventory will thus have to be monitored.

The likely retention of radioactive tritium in the PFCs of the reactor vessel is arguably the most critical safety issue in the development of ITER. One method to monitor the retained tritium in (the activated phase of) ITER is to keep track of the global gas balance in the vacuum vessel [4]. The method

---

<sup>1</sup>Also called an  $\alpha$ -particle.

<sup>2</sup>A deuterium nucleus consists of one proton and one neutron.

<sup>3</sup>A tritium nucleus consists of one proton and two neutrons.

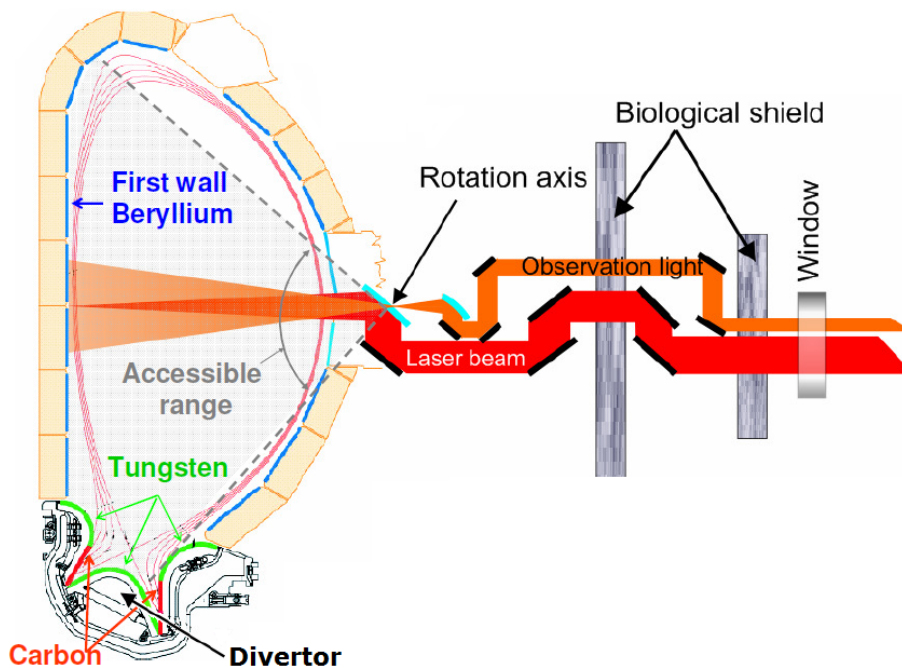


Figure 1: Cross-section of the ITER torus, demonstrating the accessible range for laser-based diagnostics. Figure obtained from Ref. [2].

of the global gas balance limits itself to the identification of the T inventory in a global way [4]. There is a call for additional diagnostic methods, as it is expected that tritium will be deposited inhomogeneously throughout the reactor [4]. It is important to locate and identify the areas within the vacuum vessel where T retention and material deposition are predominant, e.g. for establishing effective cleaning procedures [4].

One of the diagnostic methods that is being developed in parallel with the global gas balance is Laser-Induced Desorption Spectroscopy (LIDS) [2, 4, 6–9]. This method will be able to identify *in situ*, i.e. during plasma operation, the local hydrogen isotope content of the PFCs [2, 4]. LIDS relies on two processes: the desorption of retained hydrogen isotopes by a millisecond spot laser and the subsequent detection of  $H_{\alpha}$ -light emitted by the desorbed isotopes upon interaction with the plasma [2, 4]. The release of hydrogen isotopes into the plasma is vital for a successful application of the LIDS diagnostic. Therefore, LIDS is not a proper tool for measuring hydrogen isotope retention in remote areas of the ITER vessel [6]. A related diagnostic method is the Laser-Induced Desorption-Quadrupole Mass Spectrometry, or LID-QMS in short [8, 9]. In LID-QMS a quadrupole mass analyzer is used to measure the amount of material that is desorbed by the spot laser [8, 9]. The LID-QMS method is specifically designed for *ex-situ* monitoring of hydrogen isotope retention [9]. LID-QMS does not rely on plasma-interactions and is therefore a suitable method for laboratory experiments regarding laser-induced desorption [9].

For the development of LIDS as an in-situ diagnostic for ITER, it is essential to comprehend the process of desorption of hydrogen isotopes during laser spot heating. Therefore, an LID-QMS system has been set up at the Target Exchange and Analysis Chamber (TEAC) of the plasma generator Magnum-PSI [10, 11]. In this work the first principles of laser-induced desorption of hydrogen isotopes have been studied by conducting several experiments with pre-treated targets in the TEAC as well as theoretical modeling using TMAP7. Due to safety regulations tritium experiments are not allowed in Magnum-PSI. Therefore, experimental and theoretical work was restricted to LID of hydrogen and/or deuterium. It is expected that the results and observations also apply to the process of LID of tritium [12].

This paper will commence with a short, theoretical overview of LIDS and LID-QMS in Chapter 2. Topics that will be discussed are the laser heating process, the laser-desorbed area and Balmer line emissions. Laser-induced desorption was analyzed in TMAP7 using a theoretical model for a plasma-exposed tungsten sample. Chapter 3 will provide an introduction to the basic assumptions of this model. The assumptions with respect to the thermal boundary conditions and the mobile and trapped D profiles are highlighted in particular. The experimental methods are discussed in Chapter 4. At the beginning of this chapter, a schematic overview of the LID-QMS system in the TEAC is provided. The subsequent steps of the experimental procedure per LID shot are explained in Section 4.3. In Section 4.4, the two experiments that were conducted in the TEAC are introduced. The main goal and subgoals of the experiments will be clarified in this section. The results of both experiments, together with the results of the TMAP7 analysis, are given in Chapter 5. A discussion of the results follows in Chapter 6. This chapter will highlight several important aspects of the conducted work. The results are finally summarized in conclusive statements in Chapter 7. This chapter will also contain several recommendations for further research.

## 2 Theory

In the introduction, Fig. 1 elucidated how LIDS will be able to monitor a significant portion of the ITER vessel. An additional schematic overview of LIDS is given in Fig. 2.

### 2.1 Laser heating of surface

In both LIDS and LID-QMS a pulsed, millisecond laser beam is guided and imaged such that a PFC material is heated to a temperature that will allow for desorption of hydrogen impurities inside the material [13]. The maximum surface temperature  $T_{max}$  that can be achieved through laser-induced heating is given by Ref. [9]:

$$T_{max} = T_0 + \frac{2}{\sqrt{\pi}} \frac{I\sqrt{t_p}}{\sqrt{Kc\rho}} \quad (1)$$

where  $T_0$  is the initial temperature,  $I$  the intensity of the laser pulse (in  $\text{W}/\text{m}^2$ ) and  $t_p$  the laser pulse duration.  $K$ ,  $c$  and  $\rho$  are material properties representing respectively the heat conductivity, heat capacity and density of the material [9].

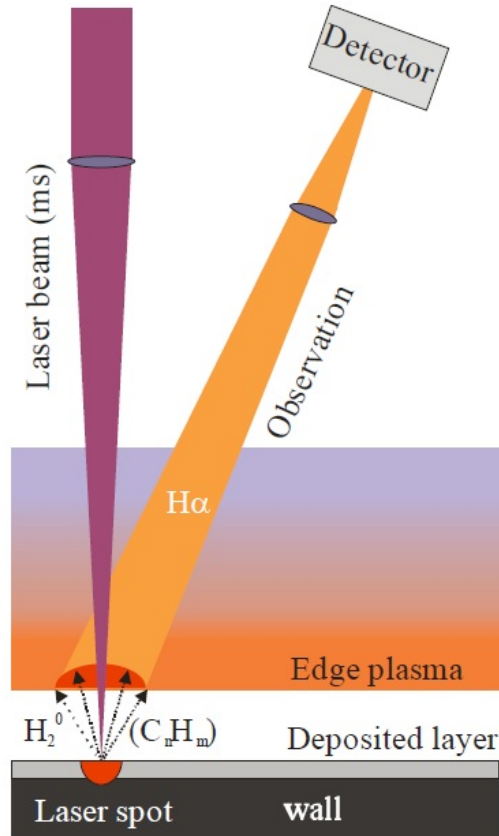


Figure 2: Schematic overview of LIDS. Figure obtained from Ref. [13].

In Table 1 some typical laser parameters for LID are shown, together with the material properties of tungsten.<sup>4</sup> For these values the maximum surface temperature is approximately 2000 K.

Laser and tungsten properties	Value
Initial temperature $T_0$	300 K
Laser intensity $I$	500 MW/m <sup>2</sup>
Laser pulse duration $t_p$	3.0 ms
Heat conductivity $K$	118 W/m/K
Heat capacity $c$	144 J/kg/K
Density $\rho$	19,079 kg/m <sup>3</sup>
Max. surface temperature $T_{max}$	2016 K

Table 1: Typical parameter values for LID on tungsten.

The (absorbed) laser intensity  $I$  is a function of the absorbed laser pulse energy  $E_{L,abs}$ , the laser irradiated area  $A_L$  and the aforementioned laser pulse duration  $t_p$ :

$$I = \frac{E_{L,abs}}{A_L \cdot t_p} \quad (2)$$

Eq. 2 is valid for an ideal laser pulse; the laser intensity is homogeneously distributed over the laser irradiated area and the supplied laser energy is constant for the entire duration of the pulse. The absorbed laser pulse energy  $E_{L,abs}$  is the laser pulse energy absorbed at the surface, i.e. it is found after the laser pulse energy at the laser output  $E_L$  has been corrected for all losses. Referring to the correction factor as  $\eta_L$ :

$$E_{L,abs} = \eta_L \cdot E_L \quad (3)$$

Last but not least, it is noted that the laser intensity can be determined retrospectively by measuring the maximum surface temperature. The laser intensity can be calculated by rewriting Eq. 1:

$$I = \frac{\sqrt{\pi}}{2} \sqrt{\frac{Kc\rho}{t_p}} (T_{max} - T_0) \quad (4)$$

## 2.2 The desorbed area

The desorbed area  $A_d$  - the area for which significant desorption occurs - is not necessarily equal to the laser irradiated area  $A_L$  due to lateral heat diffusion. In Ref. [14] the temperature profile of a circular laser spot of 2.0 mm diameter with laser intensity  $I = 1.2$  GW/m<sup>2</sup> and pulse duration  $t_p = 1.2$  ms on a tungsten surface was modeled. A contour and density plot of the temperature profile after 1.2 ms are shown in Fig. 3. A steep temperature decline can be observed at the edge of the laser irradiated area, suggesting that lateral heat diffusion is small. Therefore, the laser irradiated area will be more or less equal to the the desorbed area.

<sup>4</sup>It is assumed that  $K$ ,  $c$  and  $\rho$  are independent of temperature.

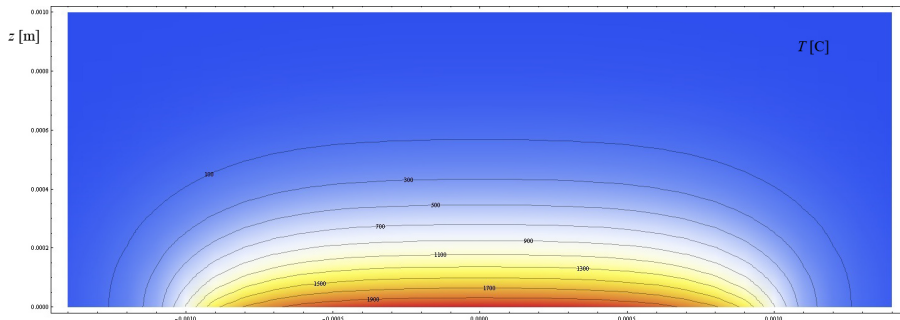


Figure 3: Temperature profile of a laser spot on a tungsten surface using the following parameters:  $d = 2.0$  mm,  $I = 1.2$  GW/m<sup>2</sup> and  $t_p = 1.2$  ms. The depth  $z$  of the sample is shown on the vertical axis;  $z = 0$  was chosen as the laser-heated surface. Figure obtained from Ref. [14].

A similar result was obtained for graphite in Ref. [8]. The temperature profile of a circular laser pulse of 1.13 mm radius was simulated. A pulse duration of  $t_p = 1.5$  ms was chosen at a laser intensity of  $I = 700$  Mw/m<sup>2</sup>. According to the simulation of Ref. [8], the graphite surface reaches a maximum temperature of 1950 K at the end of the laser pulse. Moreover, a steep temperature decline is observed at the edge of the laser irradiated, indicating equal laser irradiated and desorbed area [8]. In the following it is thus conveniently assumed that the desorbed area is approximately similar to the laser irradiated area:

$$A_d \approx A_L \quad (5)$$

The assumption of Eq. 5 has been validated in two specific cases for tungsten and graphite. For thick, multi-layer specimens - for which heat conduction towards the bulk of the material is more difficult - this assumption might introduce a systematic error in the measurements.

### 2.3 Balmer line emissions

After laser-heating of the surface, hydrogen isotopes are desorbed from the PFC material. The hydrogen isotopes are released mainly in molecular form [9]. Subsequent interaction of the desorbed species with the plasma is required in order to perform LIDS measurements. Upon their release in the plasma the hydrogen isotopes are ionized and dissociated into atoms. By electron impact the desorbed H, D and T atoms are excited to higher energy states [9]. When H atoms de-excite from the third to the second lowest energy level, they emit a photon with a typical wavelength of 656.28 nm [9]. This is known as the  $H_\alpha$  emission line and it is part of the *Balmer series* of the hydrogen atom [15]. The Balmer series result from the set of transitions of the hydrogen atom that go from higher energy states ( $n \geq 3$ ) to the second main energy level ( $n = 2$ ) [15].<sup>5</sup> As mentioned before, the transition related to the  $H_\alpha$  line is from  $n = 3$  to  $n = 2$ . The next line, the  $H_\beta$  line, is a result of the transition from  $n = 4$  to  $n = 2$ , the  $H_\gamma$  line is connected to the transition from  $n = 5$  to  $n = 2$ , and so

<sup>5</sup>The integer  $n$  is the so-called principal quantum number.

forth. Part of the Balmer line emission spectrum is represented in Fig. 4.

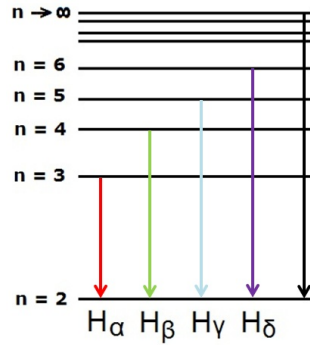


Figure 4: Balmer emission lines of hydrogen.

The nuclei of deuterium and tritium have a larger mass compared to the nucleus of hydrogen. This mass difference causes a shift in the spectral lines of the Balmer series towards shorter wavelengths for D and T [15].<sup>6</sup> This effect is known as *isotope splitting* [15]. By using a filter for the specific wavelengths of the emitted  $H_\alpha$ ,  $D_\alpha$  and  $T_\alpha$  light, the hydrogen isotopes can be distinguished from the background. The number of photons that are subsequently detected by optical emission spectroscopy have to be transformed into a total amount of H, D and T [8,9]. This can only be done in the plasma regime for which the relevant cross sections are known, by determining several conversion factors [8,9]. It goes beyond the scope of this paper to address these conversion factors in more detail.

<sup>6</sup>For example, the wavelength of  $D_\alpha$  light is 656.11 nm.

### 3 Analysis: TMAP7

The Tritium Migration Analysis Program, Version 7 (TMAP7) is the latest update of the TMAP Code [16]. TMAP was initially developed as a tool for analyzing safety issues of systems in which tritium was involved [16]. Since its design in the late 1980s, TMAP has been updated several times and has found its use in numerous applications [17].<sup>7</sup> In this work, TMAP7 has been used to study laser-induced desorption of deuterium retained on a tungsten surface. The results will be compared with LID measurements on a plasma-exposed tungsten target, although the TMAP7 analysis was not performed until after the experimental work had been completed.

#### 3.1 Modeling LID on tungsten surfaces

The model that is used for the LID simulations is an one-dimensional model of a tungsten segment with a thickness of 1.0 mm. The segment is divided into 66 nodes as illustrated by Fig. 5. At the nodes, the values of several physical quantities are determined for each instance of time. The relevant physical quantities that are calculated are the temperature, plus the mobile and trapped D concentration. The temperatures of the outer surface nodes are dictated by the imposed thermal boundary conditions. The temperatures of the other nodes follow automatically from the equations of thermal capacity and conductivity of tungsten. The thermal boundary conditions will be discussed in more detail in Section 3.2. Additionally, the initial mobile and trapped D concentrations will have to be specified, together with the number and types of traps. This is elucidated further in Section 3.3.

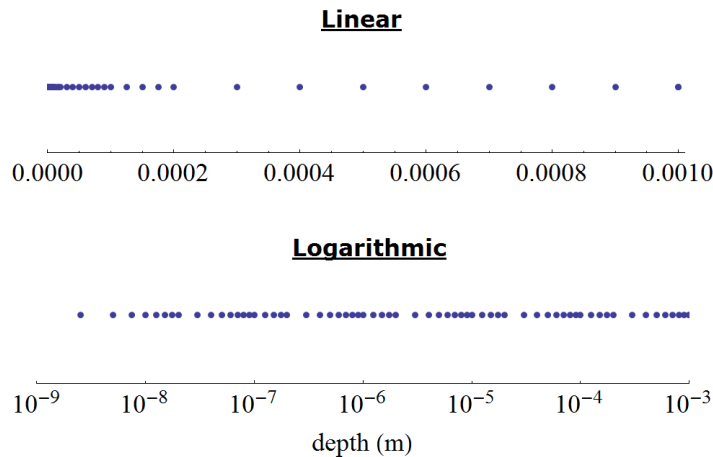


Figure 5: One-dimensional depth profile used for TMAP7, illustrated using a linear and logarithmic scale. The blue dots indicate the location of the nodes.

In the presented TMAP7 model, the tungsten segment is enclosed by a chamber with a volume of 3.0 m<sup>3</sup>.<sup>8</sup> It is assumed that the enclosure is initially filled with

<sup>7</sup>TMAP can be applied to contribute to fusion safety in ITER, e.g. as in Ref. [18].

<sup>8</sup>This is approximately equal to the volume of the TEAC.

D<sub>2</sub> gas molecules with a partial pressure of  $1.0 \cdot 10^{-6}$  Pa at a temperature of 300 K. In TMAP7, the D<sub>2</sub> gas movement across the tungsten surface is governed by two processes [16]. On the one hand, D<sub>2</sub> gas molecules adsorb to the surface. The adsorbed D<sub>2</sub> molecules subsequently dissociate into two *mobile* D atoms. In the TMAP7 model, only mobile D atoms are allowed to diffuse into the bulk of the segment [16]. On the other hand, there is the reverse process in which two mobile D atoms recombine at the surface and are released in the form of a D<sub>2</sub> gas molecule. It is thus assumed that deuterium can only be desorbed in molecular form [16].

### 3.2 Thermal boundary conditions

The initial temperature of the segment is 300 K. As soon as the simulation begins, laser heating of the left surface commences. The right surface is assumed to be uninfluenced by the laser heating of the left surface; therefore the temperature of the right surface is held constant at 300 K throughout the entire simulation. The temperature of the left boundary is dictated by a temperature profile containing linear heating and cooling, as in Fig. 6. The LID simulations have been performed for multiple temperature profiles. Each temperature profile in Fig. 6 has a similar shape, but a different maximum surface temperature  $T_{max}$  (ranging between 500 and 2000 K) in order to investigate the dependency of desorption on the laser-induced surface temperature. In each case the laser pulse has a duration of 3.0 ms, i.e. within 3.0 ms the surface heats up to  $T_{max}$ . The heating and cooling are not only assumed to progress in a linear way, but both processes are also assumed to occur within an equally long time interval. The entire simulation runs for 10.0 ms divided in time steps of 0.1 ms. The heat of the left surface is transferred into the bulk of the segment. Heat transfer in

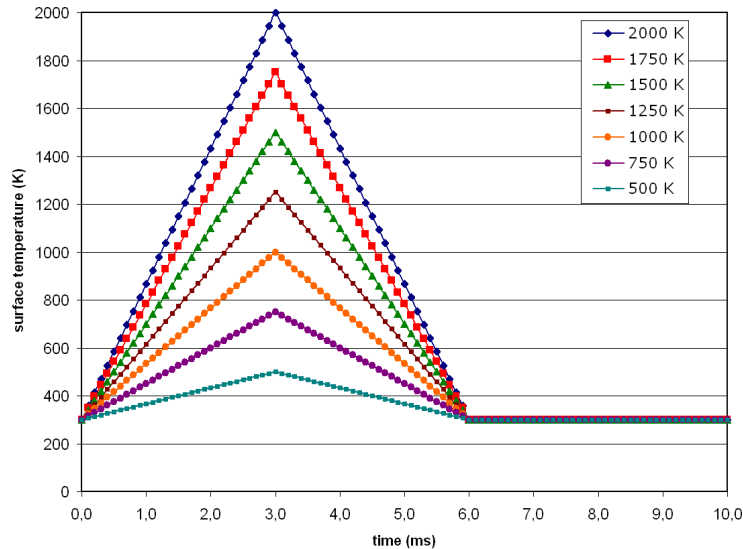


Figure 6: Temperature profiles used for TMAP7.

TMAP7 is dictated by the equation for the thermal conductivity of tungsten.<sup>9</sup>

### 3.3 Mobile and trapped deuterium

In the bulk of the segment mobile D atoms can be trapped at sites where the energy required for the mobile atoms to go to a nearby site is greater than for normal diffusion. These trapping sites typically consist of impurities, vacancies or dislocations of some sort.

From the experimental results of two plasma-exposed tungsten targets - as presented in Section 5.3 - a justification for the assumptions that are done in the remainder of this Section will appear. For the LID simulations an uniformly distributed trap was assumed with a trap release energy of 1.2 eV. The trap density  $N_t$  is chosen to be 0.05% of the lattice number density  $N$  of the tungsten segment.

$$N_t = 0.05\% \cdot N$$

The lattice number density  $N$  is calculated from the density  $\rho$ , relative atomic mass  $A_r$  and proton mass  $m_p$ :

$$N = \frac{\rho}{A_r \cdot m_p}$$

For tungsten  $\rho = 1.9079 \cdot 10^4$  kg/m<sup>3</sup> and  $A_r = 183.84$ , resulting in a lattice number density  $N = 6.28 \cdot 10^{28}$  atoms/m<sup>3</sup>. The trap density is thus determined,  $N_t = 3.14 \cdot 10^{25}$  D atoms/m<sup>3</sup>. A step function is assumed for the initial trapped D profile: up to a depth  $z_f$  the 1.2 eV traps are completely filled, in the rest of the segment the traps are empty. Taking  $z = 0$  at the left surface of the segment,  $z_f = 1.0$   $\mu$ m in the TMAP7 simulations presented in this chapter. The initial trapped D concentration  $C_t^i$  is the trap density  $N_t$  integrated over the depth  $z$ , therefore:

$$C_t^i = \int N_t(z) dz = z_f \cdot N_t = 3.14 \cdot 10^{19} \text{ D/m}^2 \quad (6)$$

It is further assumed that initially no mobile D is present within the segment.

---

<sup>9</sup>In Ref. [16] the underlying equations and theoretical model that are used in TMAP7 are discussed in more detail.

## 4 Experimental Methods

### 4.1 Overview LID-QMS in TEAC

In Fig. 7 the LID-QMS system at the TEAC of Magnum-PSI is depicted schematically. A Nd:YAG laser (LASAG FLS 352N-302) of 1064 nm is coupled to a fibre. The Nd:YAG laser is able to produce an output energy of 60 J and a laser width ranging between 0.1 to 20 ms. The laser light is guided by the fibre (50 m long, 600  $\mu\text{m}$  diameter) towards the TEAC, where the fibre output is centered by a set of plano-convex lenses which are AR coated for 1064 nm. The laser pulse is focussed at the surface of the target to a spot size of several  $\text{mm}^2$ .

The pre-treated targets are enclosed within the TEAC volume, which is about  $3 \text{ m}^3$ . In order to distinguish the LID signals from the background, a vacuum is required in the TEAC. A turbo molecular pump is able to bring the vacuum in the vessel down to  $10^{-5} \text{ Pa}$ . A movable multi-target holder (the black bar in the centre of Fig. 7) allows for an exchange of targets without intervention of the vacuum system. A very sensitive Quadrupole Mass Spectrometer (HiQuad QMG 700) equipped with an electron multiplier monitors the partial pressures inside the TEAC vessel of various pre-defined masses. The QMS analysis and sensitivity calibration are discussed further in Section 4.2.

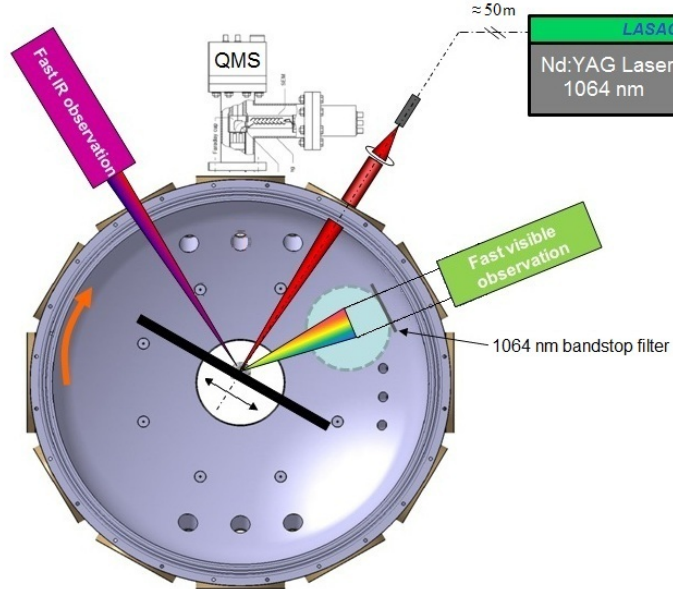


Figure 7: Schematic overview of LID-QMS in TEAC vessel.

## 4.2 QMS analysis

The QMS was used to measure both the D and H content of the pre-treated targets. As in Ref. [8], the relevant masses that were scanned for determination of the D and H content were 2, 3, 4, 16 and 20 amu. The QMS signals of these masses represent the partial pressures of H<sub>2</sub>, HD, D<sub>2</sub>, CH<sub>4</sub> and CD<sub>4</sub> respectively. The masses of H<sub>2</sub>O, O<sub>2</sub>, N<sub>2</sub> and CO<sub>2</sub> were also monitored by the QMS in order to be able to check for leaks in the TEAC. The QMS was able to scan all selected masses in approximately 0.9 s, i.e. one QMS cycle had a duration of 0.9 s.

### 4.2.1 Absolute sensitivity calibration of QMS

The output signals of the QMS are expressed in ampere (A) since the signals represent the ion currents of the individual masses. Due to variations in the ionization efficiency and transmission the sensitivity of the QMS to each mass is different [19]. In order to quantify the QMS signals of the relevant masses, calibrations were performed for H<sub>2</sub>, D<sub>2</sub> and CH<sub>4</sub>.

In order to perform the calibration, the background signals of H<sub>2</sub>, D<sub>2</sub> and CH<sub>4</sub> had to be determined first by a background measurement. The TEAC was pumped down to a low, stable pressure by the turbo molecular pump. The QMS measurement was then started. After 150 s, the valve connecting the pump and the TEAC was closed. The selected masses were monitored for another 270 s. The results are shown in Fig. 8. A linear increase in ion current is observed for all three masses. This increase in ion current (or: partial pressure) might be explained by the presence of small leaks in the TEAC and/or material release from the TEAC walls. A linear fit was made to the data and a background slope  $\Delta I_B/\Delta t$  was retrieved for each mass.

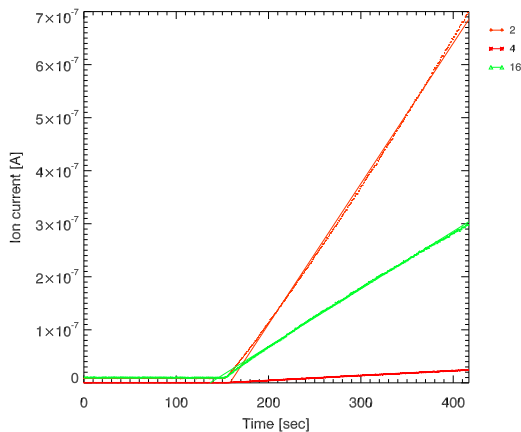


Figure 8: Background measurements and linear fits for H<sub>2</sub> (2 amu), D<sub>2</sub> (4 amu) and CH<sub>4</sub> (16 amu).

For the actual calibration measurement, a purified gas bottle of H<sub>2</sub>, D<sub>2</sub> or CH<sub>4</sub> was attached to the TEAC. Each of the gas bottles had a constant, known flow rate  $Q$ . In Table 2, the flow rate for the three gas bottles is given at room temperature. The flow rate  $Q$  is expressed in Pa·L/s. From the flow rate, the number of molecules that enter the vessel per second can be determined. This

is called the molecular flow  $dN/dt$  and is found through a simple calculation:

$$dN/dt = Q/(k_B T) \quad (7)$$

The temperature  $T$  is assumed to be equal to room temperature,  $T = 293$  K. The molecular flow rates of the  $H_2$ ,  $D_2$  and  $CH_4$  gas bottles are also listed in Table 2.

The basic procedure for the calibration measurements was as follows. Again, the TEAC was first pumped down to a low, stable pressure by the turbo molecular pump. The valve connecting the calibration leak bottle and the TEAC was subsequently opened. Both the valve of the turbo molecular pump and the valve of the calibration leak bottle are thus open. It is not possible to start the QMS measurement right after opening of the calibration leak valve. The partial pressure of the calibration gas has to stabilize first. As soon as a stable partial pressure is reached, data gathering can commence.

In Fig. 9 the calibration measurements of all three gasses are depicted. For each gas, a linear increase in ion current is observed when the valve between TEAC and pump is closed. The increase is formed by both the gas leak of the purified gas bottle and inevitable background contributions. A linear fit was made to determine the slope of the calibration graphs  $\Delta I_C/\Delta t$ . The linear fits are also depicted in Fig. 9. The slope of the calibration graph  $\Delta I_C/\Delta t$  has to be corrected for the background contributions by subtracting the earlier found background slope  $\Delta I_B/\Delta t$ . The resulting slope  $\Delta I/\Delta t$  represent the ion current signal increase due to the calibration leak bottle. The corrected slopes are listed in Table 2. From the corrected slope  $\Delta I/\Delta t$  (in A/s) and the molecular flow rate  $dN/dt$  (in molecules/s) it is possible to determine the calibration factor  $K$ :

$$K = \frac{dN/dt}{\Delta I/\Delta t} \quad (8)$$

which is then expressed in molecules/A. The calibration factors of  $H_2$ ,  $D_2$  and  $CH_4$  are found in Table 2. In Ref. [8] and [12] the calibration factor of HD was determined by the average of the  $H_2$  and  $D_2$  calibration factors. This assumption is also implemented in this paper. It is further assumed that the calibration factors of  $CH_4$  and  $CD_4$  are equal. Therefore,  $K_{HD} = 1.10 \cdot 10^{22}$  molecules/A and  $K_{CD_4} = 9.06 \cdot 10^{21}$  molecules/A. By applying the calculated calibration factors, the D and H content of targets installed within the TEAC can be obtained. In the following Section, the experimental procedure during an LID-QMS measurement is described.

Gas	Flow rate $Q$ (in Pa·L/s)	$dN/dt$ (in mol./s)	$\Delta I/\Delta t$ (in A/s)	Calibr. factor $K$ (in mol./A)
$H_2$	$3.92 \cdot 10^{-3}$	$9.6 \cdot 10^{14}$	$1.31 \cdot 10^{-7}$	$7.47 \cdot 10^{21}$
$D_2$	$1.68 \cdot 10^{-3}$	$4.1 \cdot 10^{14}$	$2.83 \cdot 10^{-8}$	$1.45 \cdot 10^{22}$
$CH_4$	$1.77 \cdot 10^{-3}$	$4.3 \cdot 10^{14}$	$4.83 \cdot 10^{-8}$	$9.06 \cdot 10^{21}$

Table 2: Calculation of calibration factors for  $H_2$ ,  $D_2$  and  $CH_4$  (note that mol. is short for ‘molecules’).

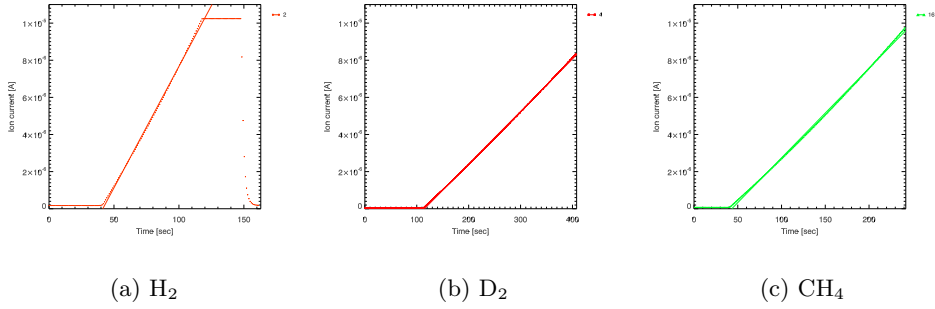


Figure 9: Calibration measurement for H<sub>2</sub>, D<sub>2</sub> and CH<sub>4</sub>.

### 4.3 Experimental procedure LID-QMS

The experimental procedure for a regular LID shot is as follows. First, the laser intensity  $I$  has to be determined for the selected maximum surface temperature  $T_{max}$ . If a certain laser pulse duration has been specified, the laser intensity can be calculated from Eq. 4. A laser pulse duration of 2 or 3 ms is usually preferred. In order to achieve the desirable laser intensity, the absorbed laser pulse energy  $E_{L,abs}$  and the laser irradiated area  $A_L$  have to be specified as well (this is elucidated by Eq. 2). The area  $A_L$  can be estimated or determined beforehand, for instance, by using burn paper or a CCD chip. From Eq. 3 it is clear that the absorbed laser energy  $E_{L,abs}$  can be calculated directly from the output laser energy if the total energy loss that occurs between laser output and target is known. The total energy loss consists of three distinctive energy losses:

1. Transmission losses in the high-energy fibre.
2. Reflection losses at the back and front of the TEAC window.
3. Laser light reflection at the target surface.

The correction factor  $\eta_L$  of Eq. 3 is therefore:

$$\eta_L = T_{fibre} \cdot T_{window} \cdot A_{target} \quad (9)$$

The three components of the total energy loss can be determined by using a laser joulemeter, although it was not applied due to time limitations. During the experimental work, each factor was estimated and based on this estimation a laser output energy was chosen.

After laser properties had been determined and targets had been installed within the TEAC, LID-QMS measurements were commenced. In this section, the procedure for a single LID shot is described. First, the TEAC was pumped down until a low, stable pressure was reached. Data recording by the QMS was then started. After 15 s, the valve between TEAC and pump was closed, leading subsequently to an increase in total pressure. A laser pulse was performed after another 30 s, often resulting in a steep increase in partial and total pressure. Data recording was continued until 30 s after the laser pulse. After termination of the QMS measurement, the valve would be opened

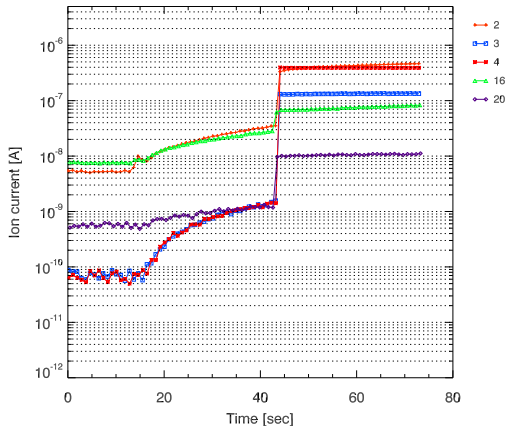


Figure 10: Example of LID-QMS measurement: QMS signal for mass 2, 3, 4, 16 and 20 over time ( $\text{H}_2$ , HD,  $\text{D}_2$ ,  $\text{CH}_4$  and  $\text{CD}_4$  resp.).

again in order to reduce the pressure to vacuum pressure. A typical LID-QMS measurement is illustrated in Fig. 10. On several occasions, background scans were made in between LID measurements in order to check for leaks in the vacuum system.

In order to determine for a species  $s$  the increase in ion current signal resulting from the laser pulse, an analysis was done using the Interactive Data Language (IDL) software [20]. Before the IDL analysis can be discussed properly, some parameters have to be defined first. The QMS cycle at which the valve between TEAC and pump is closed is called  $c_0$  and the corresponding time is  $t_{c_0}$ . At time  $t_{c_f}$  and corresponding cycle  $c_f$  the laser pulse is fired. As discussed in the previous paragraph,  $t_{c_0} \approx 15$  s and  $t_{c_f} \approx 45$  s. Between times  $t_{c_0}$  and  $t_{c_f}$  the ion current signals for the several masses grow linearly. This linear increase was already observed in the background measurement depicted in Fig. 8, but is less apparent from Fig. 10 due to the logarithmic scale of the y-axis. The linear fit routine of IDL (based on the least-squares approach) was used to determine the best fit to the ion current increase between  $t_{c_0}$  and  $t_{c_f}$  for each species  $s$ . In other words, a linear function  $I(t) = \alpha + \beta t$  was fitted for data points between cycle  $c_0$  and  $c_f$ , resulting in the best-fit values for coefficients  $\alpha$  and  $\beta$ . Subsequently, the standard deviation of this best fit was calculated:

$$\sigma = \sqrt{\sum_{k=c_0}^{c_f} (I_k - (\alpha + \beta \cdot t_k))^2} \quad (10)$$

A linear fit and standard deviation were determined for each species  $s$  ( $\text{H}_2$ , HD,  $\text{D}_2$ ,  $\text{CH}_4$  and  $\text{CD}_4$ ). If the first QMS cycle after the laser pulse is named  $c_L$ , then  $c_L = c_f + 1$  and the corresponding time is  $t_{c_L}$ . The signal  $\Delta I_s$  that can be attributed to laser-induced desorption, or LID signal, is finally calculated as:

$$\Delta I_s = I_{c_L} - (\alpha + \beta \cdot t_{c_L}) \quad (11)$$

If  $\Delta I_s < 2\sigma$ , the LID signal is considered to be insufficiently large to be distinguished from the background. For significant LID signals, the amount of

molecules  $N_s$  of species  $s$  is found by multiplication of  $\Delta I_s$  with the calibration factor  $K_s$ .

$$N_s = K_s \cdot \Delta I_s \quad (12)$$

The most important contributions to the total desorbed H are expected to come from  $H_2$ , HD and  $CH_4$ . Therefore,

$$N_H = 2N_{H_2} + N_{HD} + 4N_{CH_4} \quad (13)$$

Similarly, the total amount of desorbed D is found by adding the contributions from HD,  $D_2$  and  $CD_4$ :

$$N_D = N_{HD} + 2N_{D_2} + 4N_{CD_4} \quad (14)$$

To obtain the atomic concentrations  $C_H^d$  and  $C_D^d$  the quantities  $N_H$  and  $N_D$  respectively have to be divide by the desorbed area  $A_d$ .

$$C_H^d = \frac{N_H}{A_d} \quad \& \quad C_D^d = \frac{N_D}{A_d} \quad (15)$$

Note that the desorbed area was assumed to be equal to the laser irradiated area (recall Eq. 5).

## 4.4 LID-QMS experiments

Before the TMAP7 analysis was carried out, two separate experiments were conducted using the LID-QMS system of the TEAC; both will be described in more detail in the following Sections.

### 4.4.1 EFDA targets

For the first experiment, several pre-treated targets were provided by the European Fusion Development Agreement (EFDA). The D content of these targets was unknown, although it was assumed that the D concentration is homogeneous over each target. Identical EFDA targets were sent to several other European fusion associations, such as the Alfvén Laboratory (Sweden) and Forschungszentrum Jülich (Germany). The aim of the EFDA project was to determine the D content in D atoms/m<sup>2</sup> of each target using several, distinctive diagnostic techniques. The most noteworthy diagnostics involved in the project are Nuclear Reaction Analysis (NRA), Laser-Induced Breakdown Spectroscopy (LIBS) and LID-QMS. In this paper, the results of the LID-QMS measurements on the EFDA targets at the TEAC will be presented.

A total of 6 targets were mounted on the multi-target holder at the centre of the TEAC. An overview of the targets is given in Table 3. Targets 1 and 3 are EFDA targets consisting of diamond-like carbon (DLC) with unknown D contents 1 and 2 respectively. Targets 2 and 5 are mix-layer, EFDA targets consisting of layers of tungsten (W), carbon (C) and aluminium (Al) with unknown D contents 1 and 3 respectively. Targets 4 and 6 also have unknown D content, but are not EFDA targets.

Except for the QMS, no other diagnostics were installed for the LID measurements. A post-mortem analysis was done for targets 1 and 2, by analyzing the

Target	Description
1	DLC #1
2	Mix-layer #1 W-C-Al
3	DLC #2
4	Mix-layer W-C-Al
5	Mix-layer #3 W-C-Al
6	Balinit B12

Table 3: Target overview.

target surfaces with an optical microscope. Besides the determination of the D (and H) inventory of each target, two other subgoals were defined. The other goals of the experiment were:

1. to investigate whether it is possible to desorb the full D content of the desorbed area using a single laser shot;
2. to study the dependency of the measured D and H inventory on laser output energy.

In an attempt to achieve the first subgoal, multiple LID shots were performed on a single laser spot for targets 1, 2, 3 and 6. With regards to the second subgoal, the laser was fired onto several spots on the surfaces of targets 1 and 2, each with different laser output energy.

#### 4.4.2 Plasma-exposed targets

For the second experiment, two unpolished tungsten targets of 20 mm diameter and 1 mm thickness were exposed to a D plasma in the plasma vessel Pilot-PSI. The conditions that Pilot-PSI is able to produce ( $n_e \sim (0.1 - 10) \cdot 10^{20} \text{ m}^{-3}$ ,  $T_e \sim 1 - 5 \text{ eV}$ ), resemble the steady-state plasma conditions at the surface of the ITER divertor [14]. A schematic overview of Pilot-PSI is shown in Fig. 11; included are the target position and the applied diagnostics. A plasma beam was focussed on each target, enclosing the entire surface except for an outer edge ( $\sim 1 \text{ mm}$ ) which was covered by a clamp. A Thomson scattering system was used to determine the plasma parameters  $n_e$  and  $T_e$ . The surface temperature was monitored by a fast infrared camera (FLIR SC7500MB).

Both targets were exposed in Pilot-PSI under similar circumstances. Total plasma exposure time was about 220 s, with  $n_e = (1.0 - 2.4) \cdot 10^{20} \text{ m}^{-3}$  and  $T_e = 0.8 - 1.3 \text{ eV}$  at the centre of the plasma beam. Surface temperatures at the centre of each target varied between 130 – 225 °C. During plasma exposure, the targets were biased at a potential of -45 V.

Due to the plasma exposure in Pilot-PSI, the tungsten targets were implanted with deuterium. In an attempt to achieve resembling D distributions (and therefore a similar total D content), the conditions during plasma exposure of both targets were kept similar as much as possible. In order to investigate the impact of LID, only one of the targets was selected for further LID-QMS measurements. Thermal Desorption Spectroscopy (TDS) was then applied to both targets to determine the total D content of each sample. The main goal of

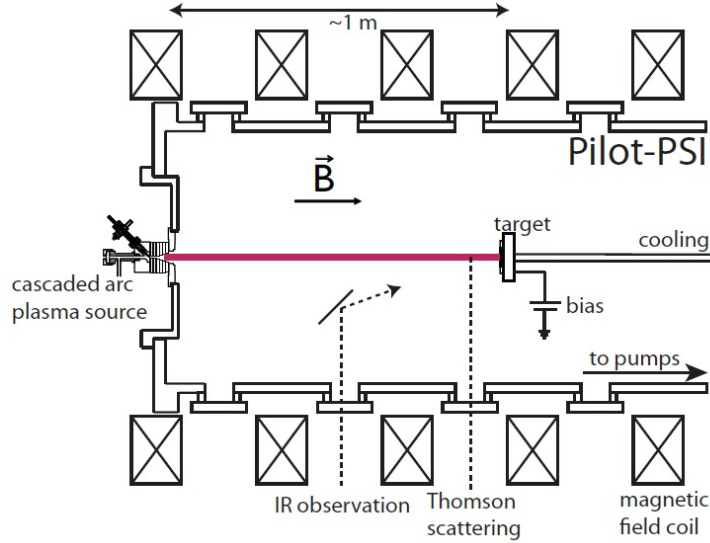


Figure 11: Schematic overview of Pilot-PSI.

the experiment was to achieve an absolute calibration of the LID-QMS system by comparing the total D content of the partially laser-desorbed target with the D content of the target without LID. Two subgoals of the experiment were also determined:

1. to obtain a radial D concentration profile of a plasma-exposed target;
2. to determine realistic assumptions for the TMAP7 analysis.

The D concentration at the centre of the tungsten target is expected to be higher than the concentration at the edge, since plasma flux is strongest there. In order to display the radial profile of the target, five LID shots were performed, as depicted in Fig. 12. The multi-target holder was not available for this experiment, and therefore the laser spot location was adjusted manually.

A fast infrared camera (FLIR SC7500MB) was installed - as depicted by Fig. 7 - in order to gain insight in realistic assumptions for the TMAP7 analysis. The fast IR camera is able to monitor the surface temperature of the target. Therefore, it was used to determine the temperature curve for heating and cooling, the maximum surface temperature  $T_{max}$  and the desorbed area  $A_d$ . The TDS measurement of the second target - without LID - was also used to support the LID analysis of TMAP7. TDS measurements consisted of heating of the entire target at a rate of 1 K per second, starting at 303 K and ending at 1273 K. Both mass 3 (HD) and 4 ( $D_2$ ) were monitored for the entire duration of the TDS measurement. The result was a profile of desorbed HD and  $D_2$  molecules versus temperature.<sup>10</sup> The shape of this profile depends on several parameters including the trap energy  $E_t$ , the trap concentration  $N_t$  and the

<sup>10</sup>By integration over the profiles of HD and  $D_2$  the total D content  $N_D$  of each target was determined through  $N_D = N_{HD} + 2N_{D_2}$ .

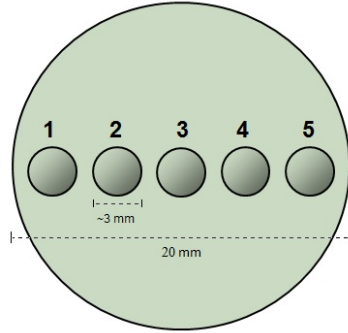


Figure 12: LID shots on plasma-exposed tungsten target as to obtain radial D concentration profile. The distance between the centres of the spots was approximately 4 mm.

trap depth  $z_f$ . The TDS measurement of the target without LID was simulated for different parameter values in TMAP7. By matching the TDS profiles of TMAP7 with the profile of the actual TDS measurement, realistic values for the trap energy, concentration and depth were determined.

A fast visible camera (Vision Research Phantom V12) was also included for the LID measurements. It was installed as in Fig. 7 to observe particle release from the tungsten surface. In principle, the optical camera can also be applied to determine the laser irradiated area  $A_L$  by placing a filter for the laser wavelength in front of the camera. The optical camera was not used for this purpose in this case. Last but not least, before the targets were subjected to TDS, the surface of both targets was studied by using an optical microscope.

## 5 Results

### 5.1 TMAP7

The time evolution of trapped and mobile D concentrations (in  $\text{D}/\text{m}^2$ ) is shown in Fig. 13 and Fig. 14 respectively for a range of maximum surface temperatures. The temperatures listed in the legends of Fig. 13 and Fig. 14 are the maximum surface temperatures  $T_{max}$ . The temperatures  $T_{max}$  are reached at exactly 3.0 ms, as was illustrated before by the temperature profiles shown in Fig. 6.

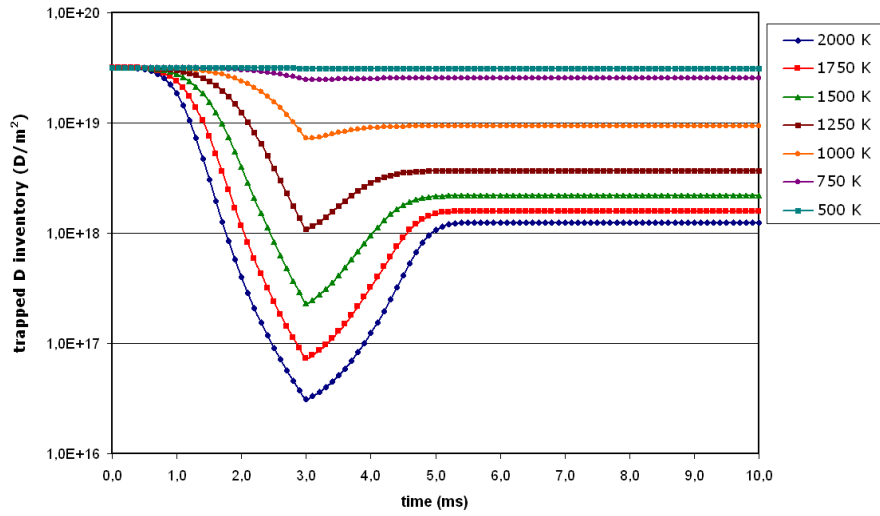


Figure 13: Trapped D inventory over time.

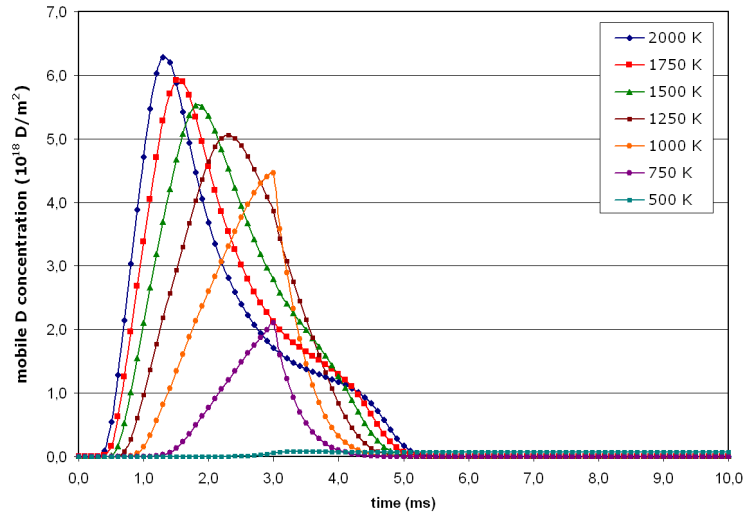


Figure 14: Mobile D inventory over time.

The initial trapped D concentration,  $C_t^i$ , amounts to  $3.14 \cdot 10^{19} \text{ D}/\text{m}^2$  for each  $T_{max}$  simulation. The trapped D concentrations decline steeply

and reach a minimum at the 3.0 ms point. Subsequent cooling of the surface results in an increase in trapped D concentrations until a stable level is achieved.

The mobile D concentrations - starting from zero - show a tendency to increase towards a maximum,  $C_m^{max}$ . Fig. 14 implies that the time required to reach concentration  $C_m^{max}$  decreases for increasing  $T_{max}$ . For  $T_{max} = 2000$  K:  $C_m^{max} = 6.28 \cdot 10^{18}$  D/m<sup>2</sup> and the corresponding time is  $t[C_m^{max}] = 1.3$  ms, i.e. long before the surface temperature reaches  $T_{max}$ . In both the 750 K and 1000 K simulation the maximum concentration is not reached within 3.0 ms. Before the mobile D concentration is able to achieve its maximum, cooling of the surface commences and this explains the discontinuities in the 750 K and 1000 K graphs. In the case of  $T_{max} = 500$  K, the trapped and mobile D concentrations are barely altered.

Another important quantity, the D surface flux, is shown in Fig. 15. The D surface flux depicted in Fig. 15 is the flux through the left surface of the segment. It appears that the D surface flux has a negative sign, indicating that there is a net D flow towards the left: deuterium is *leaving* the surface. Deuterium is desorbed from the surface in the form of D<sub>2</sub> molecules. The D surface flux in Fig. 15 is nevertheless expressed in D/m<sup>2</sup>/s. In order to find the amount of D<sub>2</sub> molecules desorbed at the surface at any moment the D surface flux of Fig. 15 has to be divided by 2.

As illustrated by Fig. 15, the outward D surface flux has a maximum value  $\Phi_D^{max}$  for each  $T_{max}$  simulation. A higher temperature  $T_{max}$  is accompanied by a greater value for this maximum. Moreover, it takes less time to reach  $\Phi_D^{max}$  in the case of higher  $T_{max}$ . In this sense,  $\Phi_D^{max}$  mimics the behaviour of the mobile D concentration  $C_m^{max}$ . From the data, it appears that the D surface flux maximum  $\Phi_D^{max}$  is reached before the mobile D concentration reaches its

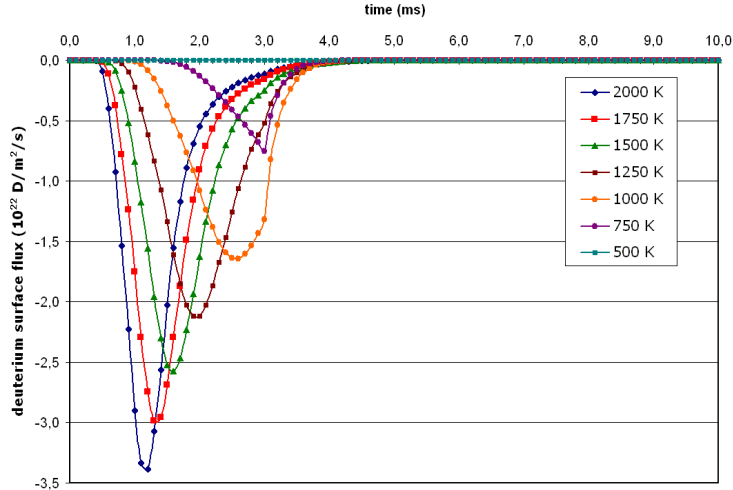


Figure 15: D flux leaving the left surface over time.

maximum,  $C_m^{max}$ . Or, written in a compact form:  $t[\Phi_D^{max}] < t[C_m^{max}]$ .<sup>11</sup> Integration of  $\Phi_D$  over the entire duration of the simulation ( $t_f = 10$  ms) results in the total amount of desorbed D per  $m^2$  by laser heating of the surface:

$$C_D^d = \int_0^{t_f} \Phi_D(t) dt \quad (16)$$

The desorption percentage  $p_d$  is then expressed as the total amount of desorbed D per  $m^2$ , as calculated in Eq. 16, divided by the initial concentration, which consisted only of trapped deuterium,  $C_t^i$ .

$$p_d = \frac{C_D^d}{C_t^i} \quad (17)$$

The desorption percentages are calculated for each  $T_{max}$  simulation and depicted in Fig. 16. For  $T_{max} = 2000$  K the desorption percentage is highest (96%), while the desorption percentages for 1500 and 1750 K are comparably high (resp. 93.1% and 95.0%).

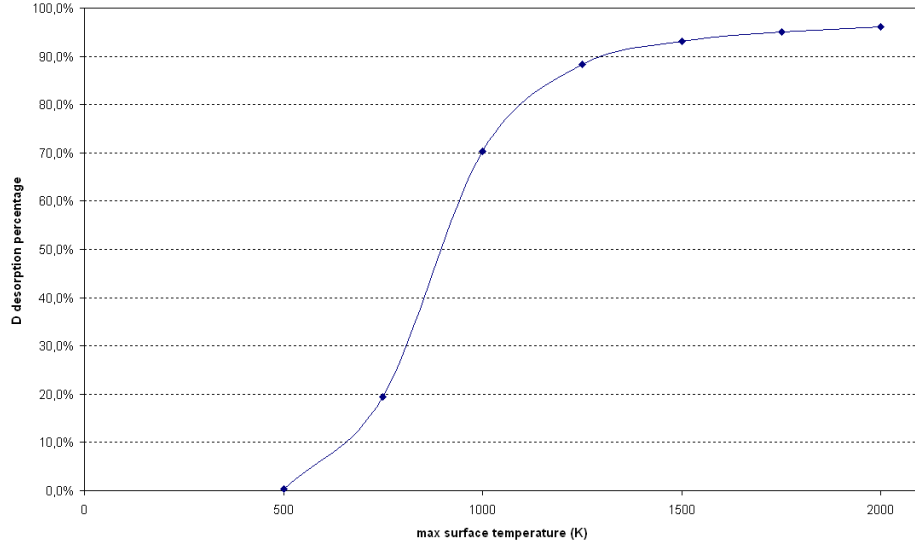


Figure 16: Desorption percentage vs maximum surface temperature  $T_{max}$ .

More information regarding the desorption process can be obtained by analyzing the evolution of the trapped and mobile D profiles of the model segment. The figures in Appendix A show the progression of the trapped D profile over time for a specific value of  $T_{max}$ . In each figure the trapped D profile is displayed at 0.0, 0.5, 1.0, 1.5, 3.0, 6.0 and 10.0 ms. Similarly, the figures in Appendix B represent the evolution of the mobile D profile over time. As is made clear from the figures, no mobile D concentration is initially present.

<sup>11</sup>Consider for example the cases for 1250 and 2000 K:  
 $T_{max} = 1250$  K:  $t[\Phi_D^{max}] = 1.95$  ms and  $t[C_m^{max}] = 2.30$  ms.  
 $T_{max} = 2000$  K:  $t[\Phi_D^{max}] = 1.20$  ms and  $t[C_m^{max}] = 1.30$  ms.

The trapped D profiles in Appendix A demonstrate a trend that is similar to the trapped D concentration of Fig. 13. The trapped D profiles progress towards a lower level until 3.0 ms. After 3.0 ms an increase in D inventory sets in until a stable level is reached. Within considerable time, the trapped D profiles begin to show a maximum at the right edge of the initial D profile and this maximum is moving further into the bulk of the segment. Deuterium is diffused deeper into the bulk for higher maximum surface temperatures  $T_{max}$  and therefore traps at a larger depth become occupied.

The fact that deuterium is diffused deeper into the bulk is a direct consequence of the increase in D mobility for increasing  $T_{max}$ . This is reflected in Appendix B, where the mobile D profiles are shown for all  $T_{max}$  simulations. Similar to the trapped D profiles, the maximum of the mobile D profiles is progressing deeper into the bulk of the segment for increasing  $T_{max}$ . The large spread in mobile D for high  $T_{max}$  causes the occupation of deep traps (up to about 10  $\mu\text{m}$ ). Finally, for each of the  $T_{max}$  simulations in Appendix B a decrease in mobile D level from 6.0 to 10.0 ms is observed. Although this decrease is only small, it appears that the system is not entirely stable during this period of time.

## 5.2 EFDA targets

An overview of the LID shots that were performed on each target is given in Table 4. The laser pulse duration  $t_p$  was 2.0 ms in each case. The laser output energy  $E_L$  was generally chosen to be lower for the DLC targets than the mix-layer targets, based on  $T_{max}$  calculations for carbon (C) and tungsten (W). The laser spots were often clearly visible on the targets, since the target surface changed colour as visualized by the images of the optical microscope shown in Fig. 19 and 20. The desorbed areas  $A_d$  of Table 4 were established by estimating the surface of these colour-changed spots. The area was assumed to be elliptical, and therefore the long and short axis of each spot were measured in order to determine the spot area.

Target	Description		# shots	$E_L$ (J)	$A_d$ (mm <sup>2</sup> )
1	DLC #1	Spot 1	4	17.7	5.2
		Spot 2	4	12.8	3.6
		Spot 3	3	10.8	5.5
2	Mix-layer #1 W-C-Al	Spot 1	4	33.5	10.4
		Spot 2	4	24.0	7.4
		Spot 3	6	20.1	6.3
3	DLC #2	Spot 1	4	17.7	5.5
4	Mix-layer W-C-Al	Spot 1	1	33.5	2.2
5	Mix-layer #3 W-C-Al	Spot 1	1	33.5	4.9
6	Balinit B12	Spot 1	8	33.5	5.5

Table 4: Overview LID shots performed per target.

In the case of target 2, the desorbed area seems to be increasing for increasing laser energy. Therefore, the assumption of Eq. 5 of similar desorbed area  $A_d$  and laser irradiated area  $A_L$  is apparently not valid for this mix-layer target. The spot areas of the other targets seem less variable (4.9 – 5.5 mm<sup>2</sup>), with some exceptions (target 1 - spot 2, target 4). In any case, the spot areas of target 1 seem to be unaffected by the increase in laser energy. The explanation for this discrepancy between targets 1 and 2 might be found in the mix-layer nature of target 2. Flaws in the connection between adjacent layers might prevent heat from penetrating deep into the bulk of the sample, resulting in an increase of lateral heat conduction.

### 5.2.1 D and H concentrations

The D and H concentrations for each target are given in Table 5. The desorbed areas  $A_d$  of Table 4 were used to determine the concentrations. The D and H inventories for targets 1 and 2 were determined from the spots with the highest laser energy. These spots were selected since - judging from Fig. 16 - the desorption percentage increases for increasing  $T_{max}$  ( $E_L$ ). The D and H inventories were determined by totalling the D and H release of the first four LID shots on each target. An exception is formed by targets 4 and 5, since only a single LID shot was performed for these targets.

Target	Description	Total D conc. (D at./m <sup>2</sup> )	Total H conc. (H at./m <sup>2</sup> )
1	DLC #1	$1.6 \cdot 10^{21}$	$1.3 \cdot 10^{21}$
2	Mix-layer #1 W-C-Al	$5.3 \cdot 10^{21}$	$4.5 \cdot 10^{21}$
3	DLC #2	$2.1 \cdot 10^{21}$	$1.4 \cdot 10^{21}$
4	Mix-layer W-C-Al	$2.2 \cdot 10^{19}$	$3.0 \cdot 10^{20}$
5	Mix-layer #3 W-C-Al	$8.2 \cdot 10^{18}$	$1.9 \cdot 10^{19}$
6	Balinit B12	$1.5 \cdot 10^{20}$	$5.2 \cdot 10^{21}$

Table 5: D and H concentration in atoms/m<sup>2</sup> of each target.

### 5.2.2 Uncertainties in D and H concentrations

The uncertainties in D and H concentrations as determined by a single laser shot can be split in uncertainties resulting from the determination of the desorbed area and uncertainties in the measured QMS signals.

**Desorbed area.** For the EFDA targets, the desorbed areas were defined from the colour-changed areas of each target. The spots were in some cases badly visible - even with optical microscopy. Several optical images will be presented in Section 5.2.5. These images will reveal that the laser spots are not perfectly elliptical. At the same time, the actual desorbed area might be slightly larger than the colour-changed area. Because of the aforementioned factors, the determined areas are considered to be rather imprecise. The total error in the desorbed areas is estimated to be approximately 15%.

**QMS signals.** The LID-QMS signals were determined by considering the masses that were assumed to be equivalent to the molecules H<sub>2</sub>, HD, D<sub>2</sub>, CH<sub>4</sub> and CD<sub>4</sub>. The most important contributions to the D and H desorption signal in the LID-QMS experiments on the EFDA targets were formed by the first three masses. Therefore, the uncertainty introduced by assuming equal ionization probabilities for CH<sub>4</sub> and CD<sub>4</sub> will be small for the EFDA targets. A larger, systematic error is expected to have been introduced by the averaging of the H<sub>2</sub> and D<sub>2</sub> calibration factors to obtain the calibration factor of HD. Another systematic error in the calibration factors is caused by the fact that the actual leak rate of the calibration bottles reduces over time (a decrease of about 1% per year). Furthermore, the mass 2 signal can be affected by water that has adsorbed to the target surface [8]. During laser exposure, this water is released from the surface and H<sub>2</sub> molecules are subsequently formed which will enhance the mass 2 signal. Last but not least, it is suggested by Ref. [8] to include the contribution of CD<sub>3</sub>H (mass 19) in the QMS analysis. For this reason, the signal for mass 19 was also monitored by the QMS during all LID experiments. LID signals for this mass were observed, but formed only a minor contribution to the total D and H signal (assuming a QMS sensitivity similar to CH<sub>4</sub> and CD<sub>4</sub>). The overall uncertainty in the LID-QMS signals is estimated to be less than 5%.

**D and H concentrations.** Based on the estimations of the uncertainties in desorbed area and LID-QMS signals, the uncertainty in the D and H concen-

trations in the case of a single LID shot is determined to be  $\sim 20\%$ . It is further possible to give an estimate for the lowest measurable target concentration of the LID-QMS system at the TEAC. During the LID measurements for both the EFDA and plasma-exposed targets, the LID signals of the QMS were clearly distinguishable from the background. From background measurements as the one in Fig. 8, the background level of mass 4 appeared to be of the order of  $10^{-9}$  A. The calibration factor for  $D_2$  was of the order of  $10^{22}$  molecules/A. The minimum number of desorbed  $D_2$  molecules still measurable by the QMS is therefore of the order of  $10^{13}$   $D_2$  molecules. This corresponds to a concentration of  $4 \cdot 10^{18}$  D atoms/ $m^2$  for a  $5 \text{ mm}^2$  spot. A rough estimate for the lowest measurable target concentration of the LID-QMS system at the TEAC is thus determined.

### 5.2.3 Multiple LID shots

Multiple LID shots were performed on the same spot (constant  $E_L$ ,  $t_p$ ) for targets 1, 2, 3 and 6. The results are depicted in Fig. 17.

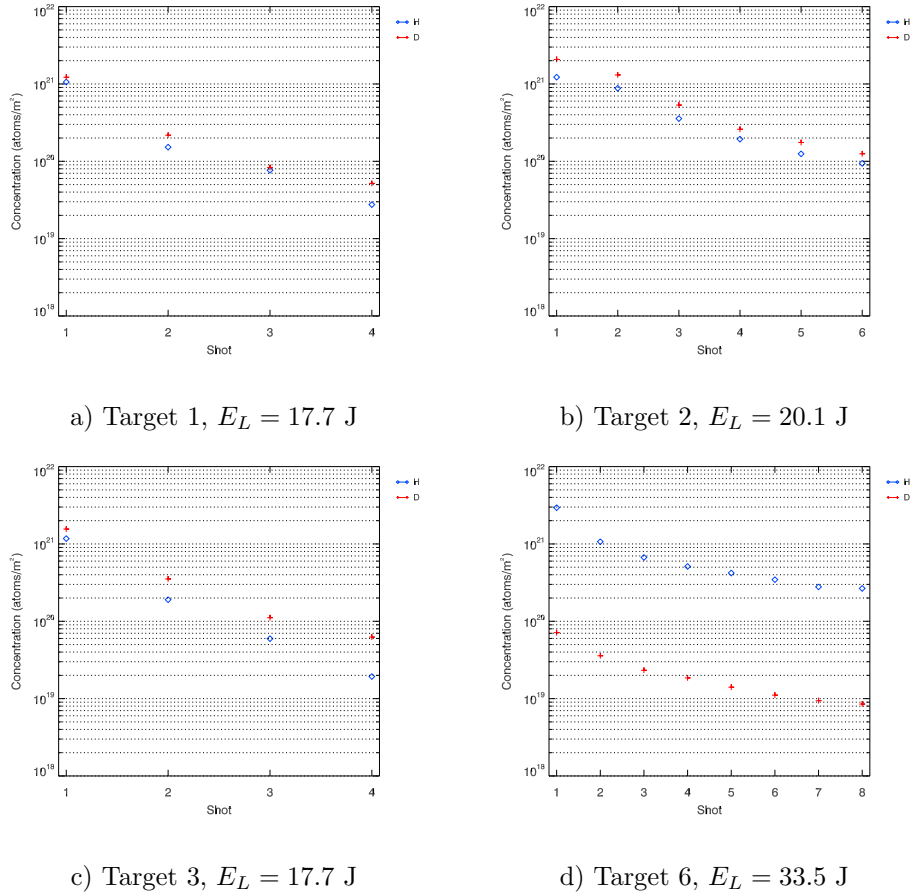


Figure 17: Multiple LID shots.

In each case, D and H release seems to be present after the first laser shot, although steeply decreasing. The decline in D and H desorption is similar for DLC targets 1 and 3. In both cases, the D release of the second laser shot is about 20% of the D release of the first laser shot. For the fourth and final laser shot this percentage is about 4%. For targets 2 and 6, the D desorption of the second laser shot as percentage of the D desorption of the first laser shot is 63% and 50% respectively. These percentages are much higher than for the DLC targets. After six laser shots, the D release of target 2 is 6% of the first LID shot. For target 6, percentages are still higher than 10% after 8 laser shots.

For the laser shots performed after the first shot, two factors influence the resulting D and H signals. The first factor is caused by an altering reflection coefficient due to the change in surface colour and morphology. The second factor is the occurrence of lateral D diffusion. Both factors are able to enhance the D and H signals for multiple laser shots. Laser light absorption was possibly increased due to roughening and blackening of the surface. At the same time, D might diffuse towards the laser spot during or after laser exposure due to the lower D concentration there. For target 2, the higher percentage of the second shot can be explained by the fact that the laser energy (20.1 J) was low and therefore the D inventory was not fully desorbed by the first shot. If the spot on target 2 with the highest laser energy (33.5 J) is considered, the second laser shot amounts to 25% of the first laser shot. This percentage is similar to the found percentages for the second LID shot of targets 1 and 3 ( $\sim 20\%$ ). The question is what part of this 20% can be contributed to the higher laser light absorption and/or lateral diffused D. Unfortunately this presently involves speculation, and therefore additional experiments are required (Section 7.1).

**Additional uncertainty.** In Table 5 the D and H concentrations of targets 1, 2, 3 and 6 were obtained by summing the contributions of multiple LID shots. As was discussed above, this might introduce additional error in the observed concentrations. Moreover, an equal desorbed area was assumed for all these shots. Variations in desorbed area between subsequent laser shots consequently involve a deviation of the calculated concentrations from the actual concentrations. The uncertainty in the D and H concentrations of Table 5 - at least, the ones that were determined by summing the QMS signals of multiple LID shots - is estimated to be approximately 25%.

#### 5.2.4 Laser output energy $E_L$

In Fig. 18 the observed D and H concentrations of targets 1 and 2 are shown for several laser output energies. In both cases, desorption increases for higher laser output energy. It is difficult to compare Figures 18a and 18b, due to the differing material properties of both targets. Recall that target 1 consisted of DLC and that target 2 was a mix-layer W-C-Al target. As a consequence of several  $T_{max}$  calculations for C and W, higher laser energies were chosen for target 2. An important factor in explaining the differing energy ranges is the difference in reflectivity between both targets, i.e. the reflectivity of target 2 was estimated to be higher than the reflectivity of target 1. For the highest laser energy chosen for each target (17.7 J and 33.5 J for targets 1 and 2 respectively),

the estimated temperature  $T_{max}$  was 2000 K in both cases. For target 1 there appears to be a sharp threshold value between 11 and 13 J. Desorption is still significant for 12.8 J, but the signal drops several orders of magnitude for the 10.8 J laser shot. It is observed in Table 4 that the desorbed area of spot 2 of target 1 is rather small compared to the areas of spot 1 and 3. By assuming  $A_L \approx A_d$ , this is an indication that the laser intensity, and thus the maximum surface temperature, might have been relatively high. This therefore accounts for the signal drop between spot 2 (12.8 J) and spot 3 (10.8 J).

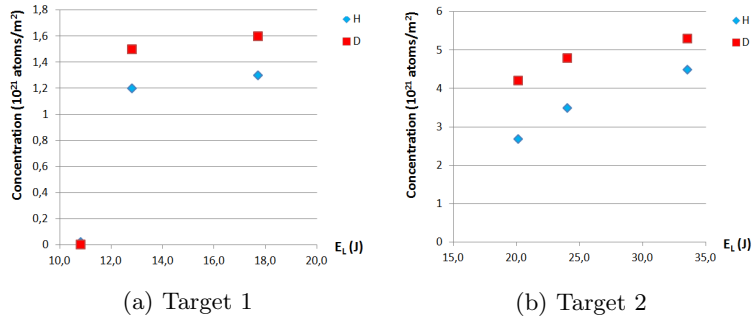


Figure 18: Atomic D and H concentration vs laser output energy  $E_L$ .

For target 2 the increase of D and H desorption for higher  $E_L$  is more continuous. In principle, it would have been preferable to obtain a graph of the D and H concentrations versus  $T_{max}$ . The shape of this graph could then have been compared with the shape of Fig. 16 obtained from TMAP7, which shows the desorption percentage as a function of temperature  $T_{max}$ . Since the fast IR camera was not installed for the EFDA experiments and laser energy losses were unknown, it was not possible to determine the maximum surface temperature  $T_{max}$  for each spot. Recall that the EFDA experiments were conducted before the TMAP7 analysis.

### 5.2.5 Optical microscopy

Surface images of the three laser spots of targets 1 and 2 were made by an optical microscope. In Fig. 19 and 20 the green bar represents a length of 1.0 mm; all images have been made with  $5\times$  enlargement.

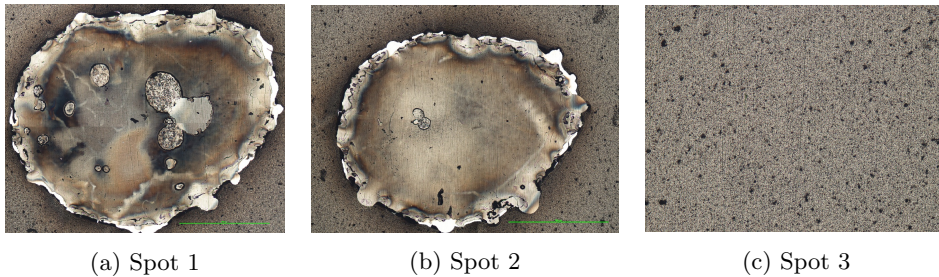


Figure 19: Optical microscope images of target 1.

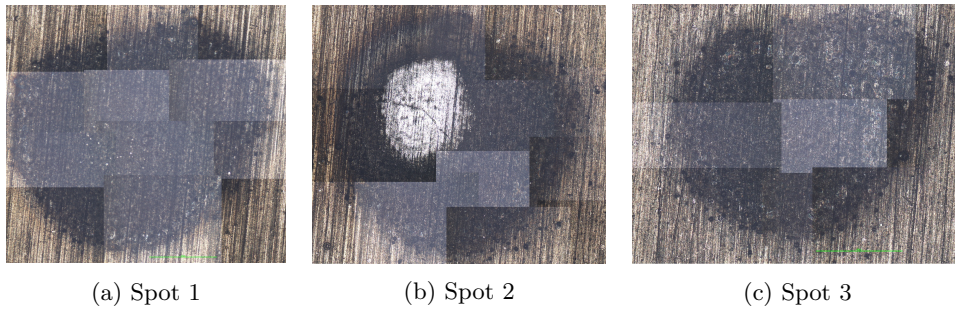


Figure 20: Optical microscope images of target 2.

For the laser energies used at spot 1 and 2 of target 1 (Fig. 19a & 19b), surface melting seems to have occurred. The 10.8 J applied for the third laser spot (Fig. 19c) was not sufficient for surface melting and, consequently, the desorbed area was badly visible. As was already seen in Fig. 18, desorption was negligible for this laser spot.

The spots of target 2 show a change in surface colour, but the underlying structure has remained more or less intact. The white dot in Fig. 20b emerged as a result of a LIBS measurement performed on the same spot. Ignoring the white area of spot 2, the surface morphology of all three spots is similar but - as was observed in Table 4 - the spot areas of target 2 increase significantly for increasing  $E_L$ .

### 5.3 Plasma-exposed targets

An overview of the number of LID shots and the determined desorbed areas  $A_d$  for the plasma-exposed target are shown in Table 6. The first spot was used as a test spot to align the laser and to determine a proper laser energy. Spots 2 to 6 were chosen to lay on the same line through the centre of the target. As in Fig. 12, spot 2 is the outer left spot and spot 6 the outer right spot. For spots 2 to 6, 3 laser shots were performed, each with a laser output energy of 28.2 J and laser pulse duration of 3.0 ms. The laser-heated or desorbed areas  $A_d$  per subsequent spot are given in Table 6. The surface areas were determined by analysis of the IR images. The boundaries of the laser-heated area were defined at 550 °C ( $\approx$  800 K). From Fig. 16 the desorption for this temperature is about 25% of the total D concentration. Using this definition, the areas per LID shot seem to vary significantly throughout the measurements. Also, the maximum surface temperatures determined by the IR camera were measured within a wide range, between 1000 – 1700 K. From the IR graphs, it was possible to determine the maximum temperature as a function of time. It was observed that time for heating and cooling was about equal and that both heating and cooling were not far off from being a linear process, as was assumed in Section 3.2. Last but not least, no material release from the target surface was observed by the fast camera images.

Spot	# shots	$A_d$ (mm <sup>2</sup> )
1	4	17.9; 9.1; 7.6; 6.4
2	3	5.1; 5.1; 5.1
3	3	6.8; 18.7; 7.6
4	3	7.1; 8.1; 5.5
5	3	5.6; 6.6; 8.1
6	3	7.6; 8.1; 8.1

Table 6: Overview LID shots performed on target.

#### 5.3.1 Uncertainties in D and H concentrations

Following a similar reasoning as in Section 5.2.2, the uncertainty in the D and H concentrations in the case of a single LID shot during the plasma-exposed target experiments is estimated to be  $\sim$ 20%. This uncertainty is again split into uncertainties related to the desorbed area and uncertainties in the LID-QMS signals.

**Desorbed area.** The surface areas of the laser spots on the plasma-exposed target were determined by analysis of the images of the fast IR camera. As shown in Table 6, this analysis reveals variations in surface area over all laser shots. The variations between laser spots are likely to be the result of the manual adjustment of the laser when moving to a new laser spot. This manual operation also occurred on two occasions during LID measurements on the same spot (spot 1 and 3). The smaller fluctuations in desorbed area per spot can possibly be explained by inaccurate measurement of the desorbed area due to the (low) quality of the IR images. The uncertainty in desorbed area is thus estimated to be 15%.

**QMS signals.** Several uncertainties regarding the LID-QMS signals were already discussed in Section 5.2.2. These uncertainties are also valid in the case of the plasma-exposed target experiments, with the exception of the uncertainty introduced by assuming equal ionization probabilities for  $\text{CH}_4$  and  $\text{CD}_4$ . This contribution is considered to be negligible in this case. For the plasma-exposed target, the main contributors to the D and H signals were mass 3 and 4 ( $\text{HD}$  and  $\text{D}_2$ ). One would expect both the  $\text{CH}_4$  and  $\text{CD}_4$  signal to be negligible for the plasma-exposed target, since the LID shots were performed on a tungsten target. Indeed, not a single  $\text{CD}_4$  signal was measured for the plasma-exposed target and contributions from mass 16 ( $\text{CH}_4$ ) were small.

Furthermore, an additional uncertainty was introduced for the LID measurements on the plasma-exposed target since no calibration was performed for these measurements. The old calibration data of the EFDA targets were used instead. The sensitivity of the QMS can change with time or when the general settings of the device are changed (in this case, the QMS settings were unaltered). Nonetheless, the uncertainty in the LID-QMS signals is again estimated to be less than 5%.

### 5.3.2 Radial D concentration profile

Due to the wide variation in desorbed area per laser spot, it was decided to base the D and H concentration (in  $\text{at./m}^2$ ) of each laser spot on the first LID shot. The radial profile (spots 2 to 6) is visualized in Fig. 21. As expected, the D concentration is higher in the centre than at the edges. The D concentration for the middle spots is at around the same level, in the range of  $(3.5 - 4.0) \cdot 10^{19}$  D atoms/ $\text{m}^2$ . The initial D concentration that was assumed for the TMAP7 analysis was of similar order,  $C_t^i = 3.14 \cdot 10^{19}$  D/ $\text{m}^2$  according to Eq. 6.

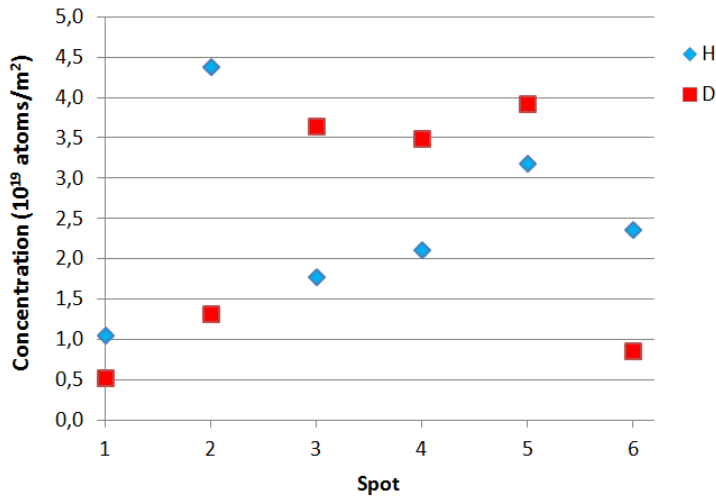


Figure 21: Radial D (and H) concentration profile.

Regardless of the uncertainties in the D concentrations that were already discussed in Section 5.3.1, it is expected that the actual concentrations at the centre of the target will be higher than the aforementioned range of  $(3.5 - 4.0) \cdot 10^{19}$  D atoms/m<sup>2</sup>. For the temperatures that were observed by the fast IR camera (1000 – 1700 K), it is likely that not all D was desorbed by the first laser shot. The corresponding desorption percentages can be extracted from Fig. 16. For the 1000 – 1700 K temperature interval the desorption percentages range between 70% and 95%. The actual concentration is therefore estimated to be in the range of  $(3.7 - 5.7) \cdot 10^{19}$  D atoms/m<sup>2</sup>.

### 5.3.3 TDS

**Trap parameters.** The trap parameters of Section 3.3 were determined by comparing the TDS analysis done in TMAP7 (Fig. 22a) with the TDS profile of the actual TDS measurement on the target without LID (Fig. 22b). The D release from a certain trap will appear in the TDS spectrum as a Gaussian distribution. The TDS analysis of TMAP7 for a trap with  $E_t = 1.2$  eV,  $z_f = 1.0$   $\mu$ m and  $N_t = 0.05\% \cdot N$  reveals a Gaussian with its maximum value at  $T = 524$  K. The surface flux at this point reaches a value of about  $2.0 \cdot 10^{17}$  D<sub>2</sub> molecules/m<sup>2</sup>. Multiplying this maximum with the surface area of the 20 mm diameter target, results in a maximum D release of  $6.3 \cdot 10^{13}$  D<sub>2</sub> molecules. The D profile of the TDS measurement is the result of the sum of two Gaussian distributions (Fig. 22b). The most important contribution comes from a Gaussian with a maximum value of  $7.0 \cdot 10^{13}$  D<sub>2</sub> molecules at a temperature of 512 K. These values correspond with the values as determined in the TMAP7 analysis. It was thus assumed that the conditions that were set in the TMAP7 analysis of Section 3.3 were realistic conditions for the examined targets. Nevertheless, it can not be ruled out that other combinations of  $E_t$ ,  $z_f$  and  $N_t$  exist that result in a similar, fitting TDS profile.

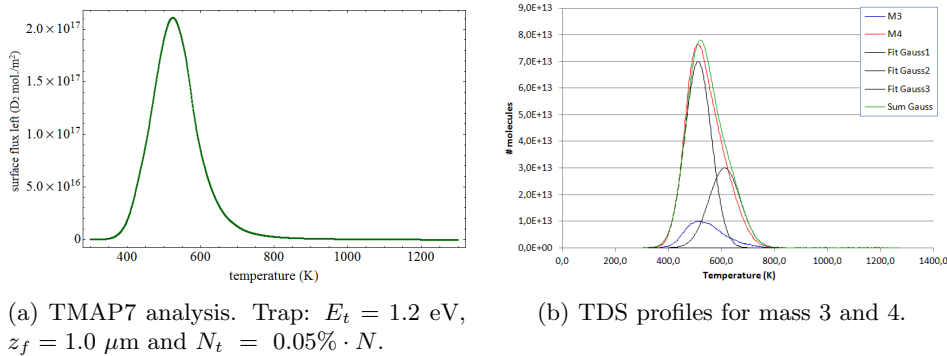


Figure 22: TDS results.

**Absolute calibration LID-QMS.** The total amount of released D and H atoms were determined for the LID measurement on target 1. The contributions of all six spots were taken into account to determine the total D and H desorbed from the target. By comparing this amount with the total D release from target

1 and 2 in the TDS measurement an absolute calibration was hoped to be achieved. The results are displayed in Table 7. The D release during the TDS measurement of the target with LID is found to be higher than the D release for the target without LID.

Measurement	Released D (in $10^{16}$ D atoms)	Released H (in $10^{16}$ H atoms)
LID target 1	0.12	0.11
TDS target 1	2.93	–
TDS target 2	2.64	–

Table 7: Overview total desorbed D and H atoms per measurement.

The variation in D content of two targets that have been through a similar plasma-exposure sequence in Pilot-PSI is estimated to be 10-15 %. The total D content of the plasma-exposed target with LID is determined at  $(2.93 + 0.12) \cdot 10^{16} = 3.05 \cdot 10^{16}$  D atoms, which is 15.5% higher than the D content of the target without LID. Therefore, an absolute calibration of the LID-QMS system at the TEAC is not possible. For the absolute calibration to work, both targets should have similar D content ( $< 1\%$  difference). Also, the LID signal is rather small compared to the total D content as determined by the TDS measurements. The LID signal could have been enhanced by increasing the total number of laser spots on the target and by using higher laser energies.

#### 5.3.4 Optical microscopy

Again, an optical microscope was used to study the surface of both plasma-exposed targets. The images of Fig. 23 were made with  $5\times$  enlargement so that the green bar represents a length of 1.0 mm. Unlike the laser spots on the EFDA targets, the spots on the plasma-exposed target with LID were badly detectable with the optical microscope. No colour change of the surface has occurred for the LID target. By comparing the surface of the target with LID to the target without LID (Fig. 23a and 23b respectively), a difference in surface morphology was observed. For the laser desorbed areas of the LID target small cracks have appeared in the surface.

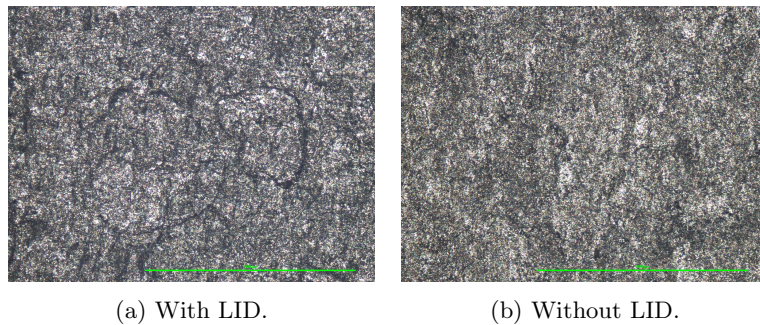


Figure 23: Optical microscope images of both plasma-exposed targets.

## 6 Discussion

Several aspects from this paper will be discussed below. An important aspect that will be discussed first is the behaviour of the curves of the trapped D concentration, the mobile D concentration and the D surface flux generated in TMAP7. A physical explanation for the observed results will be given. Another noteworthy aspect is the problem of determining the desorbed area  $A_d$ ; this area is essential for obtaining the hydrogen isotope concentrations. Finally, a more extensive comparison is made between the TMAP7 analysis and the experimental results regarding the plasma-exposed target.

### 6.1 Physical background of TMAP7 results

The evolution of the trapped D concentration, the mobile D concentration and the D surface flux in time was described and illustrated (Fig. 13, 14 and 15 resp.) in Section 5.1. The specific behaviour demonstrated by these quantities will be discussed below.

A comparison of Fig. 13 with Fig. 6 suggests that the trapped D concentration mimics the behaviour of the maximum surface temperature profile. In other words, the trapped D concentration is strongly temperature dependent. If temperature increases, trapped D becomes mobile and the total amount of trapped D is diminished. The mobile D concentration, on the other hand, does not follow the temperature profile so strictly as the trapped D concentration. The total mobile D concentration is determined by two processes:

- supply of mobile D by release of trapped D;
- loss of mobile D due to desorption from the surface.

It was assumed that there is no mobile D present in the sample at the start of the simulation. Therefore, initially the loss of mobile D through desorption is low. Mobile D concentration increases rapidly due to supply of mobile D from the D traps. It is observed from Fig. 14 and 15 that loss by desorption becomes more significant as the mobile D concentration increases. At the maximum of the mobile D curve, the supply from trapped D is balanced by an equal D desorption.

The behaviour of the D surface flux is more difficult to explain. The D surface flux depends on the temperature of the sample and the availability of mobile D. The dependency on temperature can be split in two distinguishable factors. An increasing temperature:

- allows more mobile D atoms to overcome the required potential to escape the surface;
- involves an increase in mobile D concentration by release from the D traps.

In the case of the second factor, a larger amount of mobile D is then available for desorption. Furthermore, the availability of mobile D is also separated into two factors. The availability of mobile D depends on:

- the total D concentration;

- the overall D profile.

The first factor is obvious; a small, initial D concentration results in a small outward D flux. The second factor hints at the fact that D at large depth is harder to desorb than D adjacent to the surface. With these factors in hand, it is possible to give an explanation for the behaviour of the D surface flux curve of Fig. 15. Initially, both the mobile D concentration and temperature increase. Consequently, there is a rapid increase in the outward D flux. This outward D flux causes a steep decline in the total D concentration, which becomes more and more exhausted. Moreover, it was observed in the D profiles of Appendix A and B that a small part of the mobile and trapped D is diffused deeper into the bulk of the material. The result is that the outward D flux may start to decline even though surface temperature is still rising. As an example, the LID simulation for  $T_{max} = 2000$  K is analyzed in more detail. In this case, the D surface flux reaches a maximum after 1.2 ms. The balance occurs long before  $T_{max}$  is reached ( $T \sim 980$  K for  $t = 1.2$  ms). At this point, already 66.3% of the initial D concentration has been desorbed. This relatively small D concentration, which has partially diffused inwards, is the cause for the decrease in outward D flux.

## 6.2 Determination of desorbed area $A_d$

A large uncertainty in the experimental results resides from (the imprecise determination of) the desorbed area  $A_d$ , which is essential for obtaining the D and H concentration of the targets. First of all, it should be noted that there was a difference in the determination of the desorbed areas between the two experiments. For the EFDA targets the desorbed area was defined from the *colour-changed areas* of each target. As a result, the determined areas were rather imprecise. On the other hand, the desorbed areas on the plasma-exposed target were determined by the *laser-heated area*. This laser-heated area was obtained from the temperature profile of the surface by analysis of the IR images and its boundary was chosen rather arbitrarily at 550 °C ( $\approx 800$  K). For this temperature the desorption percentage is about 25%. This IR-based analysis revealed variations in surface area over all laser shots; the uncertainty in the desorbed area was again estimated to be large ( $\sim 15\%$ ).

From the discussion above it should be clear that it is difficult to define the desorbed area  $A_d$ . In Section 2.2 it was argued that the desorbed area  $A_d$  should - at least - be similar to the laser irradiated area  $A_L$ . In Section 5.2 it was suggested that this is not always the case: for target 2 of the EFDA targets the colour-changed area increased for increasing laser energy and constant  $A_L$ . To account for the desorbed area  $A_d$  in a proper way, a comparison should be made between the laser irradiated area (measured by a CCD chip), the colour-changed area (preferably determined from the images of an optical microscope) and the laser-heated area (determined from the IR images) for each LID spot. This comparison will reduce the uncertainty in the desorbed area. Reducing the uncertainty in desorbed area is essential when a fair comparison of concentration levels of the laser spots is to be made. Moreover, by comparing the three aforementioned areas, a more clear definition of the desorbed area can hopefully be given.

### 6.3 Comparison TMAP7 and experiment

The TMAP7 analysis was carried out after both the EFDA and plasma-exposed target experiments had been conducted. For this reason, a comparison between experimental work and TMAP7 was lacking in some cases. For example, in Section 5.2.4 it would have been preferable to obtain a graph of the D and H concentrations versus  $T_{max}$ . The shape of this graph could then have been compared with the shape of Fig. 16 obtained from TMAP7, which shows the desorption percentage as a function of temperature  $T_{max}$ .

A quantity that can be compared with results from TMAP7 is the D concentration of the middle spots of the radial D profile that was obtained in Section 5.3.2. The actual concentration of the middle spots of the radial D profile was estimated to be in the range of  $(3.7 - 5.7) \cdot 10^{19}$  D atoms/m<sup>2</sup>. A comparison of TDS analysis in TMAP7 with TDS measurements revealed the following trapping parameters (to be used for the LID analysis in TMAP7):  $E_t = 1.2$  eV,  $z_f = 1.0$   $\mu\text{m}$  and  $N_t = 0.05\% \cdot N$ . For these trapping parameters, the initial D concentration was calculated in Section 3.3,  $C_t^i = 3.14 \cdot 10^{19}$  D/m<sup>2</sup>. The estimate for the actual concentration level and the calculated concentration in TMAP7 do not correspond. One explanation for this difference is that - although the trapping parameters were assumed to be realistic - it can not be ruled out that other combinations of  $E_t$ ,  $z_f$  and  $N_t$  exist that would have resulted in a similar fit between TMAP7 analysis and TDS measurement. This other combination would consequently have a different, corresponding initial D concentration  $C_t^i$ . A second explanation involves the presence of an additional trap in the plasma-exposed target. From the TDS desorption profile another Gaussian appeared ("*Fit Gauss2*" of Fig. 22b) with the maximum at 611 K, indicating an additional trap concentration in the target. If this additional trap is included in the TMAP7 analysis, this will automatically result in a higher initial D concentration.

Finally, it is noted that the assumption done in the TMAP7 analysis of the absence of an initial mobile D concentration specifically applies to samples with significant time between plasma-exposure and LID. For an LIDS measurement, the sample is likely to be infused with mobile D from the plasma. It is expected that this will add another complexity to the analysis of LIDS measurements.

## 7 Conclusion

In this work the first principles of laser-induced desorption of hydrogen isotopes residing on PFC materials have been studied. Several experiments were conducted with pre-treated targets in the TEAC of Magnum-PSI as well as theoretical modeling using TMAP7.

The theoretical modeling of the TMAP7 analysis was done for a tungsten sample with a D profile that was obtained by analysis of TDS measurements on a plasma-exposed target. The focus of the TMAP7 analysis was mainly on determining the influence of maximum surface temperature on the amount of desorption (expressed as a percentage of the initial D concentration). For a 3.0 ms laser pulse, it was observed that desorption percentages for  $T_{max} \geq 1300$  K are higher than 90%. From the TMAP7-generated curve showing desorption percentage as function of  $T_{max}$ , it was also observed that deviations in these high maximum surface temperatures result in small deviations in desorption percentage. This is an important argument in favour of using high laser energies in LID measurements, for which surface temperatures may vary due to deviations in laser energy or spot size. Last but not least, the TMAP7 analysis has proven itself as a valuable contribution to the study of LID by revealing the significant processes that occur during laser exposure.

The D and H concentrations of four EFDA targets, as well as of two other samples with unknown hydrogen isotope content, were determined by using an LID-QMS system that was installed for this purpose at the TEAC of Magnum-PSI. The determined D and H concentrations consist of the sum of the D and H signals of the first four laser shots for each laser spot, since it was assumed that the local D and H in the sample were only partially desorbed by the first laser shot. The desorption percentage curve generated in TMAP7 seems to support this assumption. Several uncertainties were appointed with respect to the concentration values. The most important error is expected to come from the determination of the desorbed area. The desorbed area is essential for obtaining the D and H concentrations of the targets and therefore an important aspect of further study will be to deal with the uncertainties in the desorbed area. Finally, for multiple LID shots with high laser energies, it was observed that the D desorption caused by the second laser shot on the same laser spot amounts to about 20% of the D desorption related to the first laser shot.

Two tungsten targets were exposed to a D plasma in the plasma device Pilot-PSI under similar conditions. By performing several LID measurements in the TEAC on one of these targets a radial D concentration profile was determined based on the first laser shot on each spot. The D concentration of the middle spots seemed to be at around the same level, while the concentration at the edges was significantly lower. After the LID measurements, the total D content of the targets was determined by TDS and both values were subsequently compared in order to obtain an absolute calibration for the LID-QMS system of the TEAC. It appeared that the variation in D content of the two plasma-exposed targets was too large to achieve an absolute calibration of the LID-QMS system. The D content of the plasma- and laser-exposed

target was actually found to be 15.5% higher than the D content of the target that was not laser-exposed. Last but not least, some very insightful results were obtained by comparing the TDS profile of the plasma-exposed target without LID with several TDS simulations done in TMAP7. This comparison revealed the following, realistic trapping parameters:  $E_t = 1.2$  eV,  $z_f = 1.0$   $\mu\text{m}$  and  $N_t = 0.05\% \cdot N$ . These trapping parameters were subsequently applied to the LID analysis in TMAP7. Unfortunately, it is possible that other combinations of  $E_t$ ,  $z_f$  and  $N_t$  exist that would have resulted in a similar fit between TMAP7 analysis and TDS measurement. Also, the TDS measurement indicated the presence of an additional trap concentration in the target. These last two factors form a possible explanation for the difference that was observed between the initial D concentration as calculated in TMAP7 and the observed D concentration at the middle spots of the plasma-exposed target.

## 7.1 Recommendations for further research

The specific characteristics of laser-induced desorption of hydrogen isotopes from PFC materials (tungsten in particular) should be explored in more detail in future research by using both theoretical models and experiment.

The LID analysis of TMAP7 could be expanded by including additional traps, such as the trap observed in the TDS profile of the plasma-exposed target, or by including a hydrogen concentration in the sample. The TMAP7 analysis could furthermore be applied to simulate multiple LID shots by using the final trapped and mobile D profiles as input for the next LID simulation. Also, the effect of laser pulse duration on total D desorption can be investigated, i.e. to determine if desorption can be increased significantly by increasing the pulse duration.

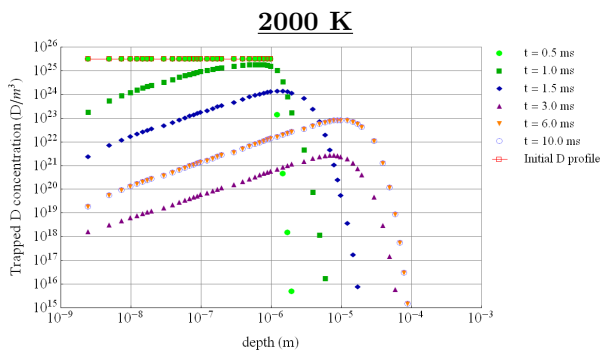
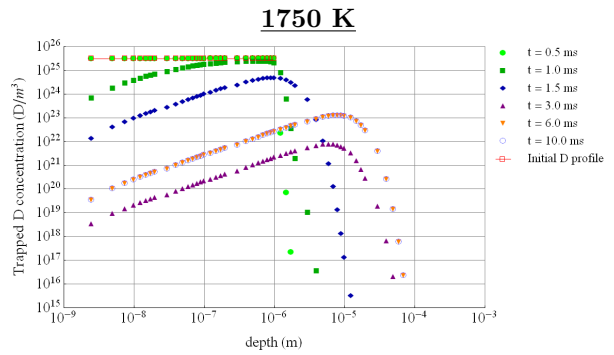
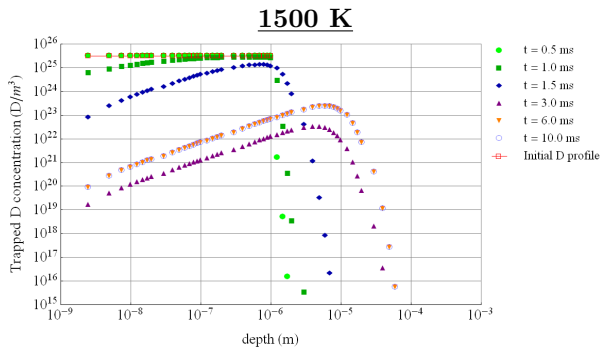
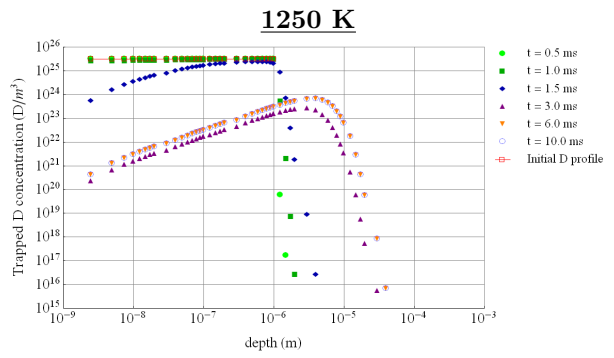
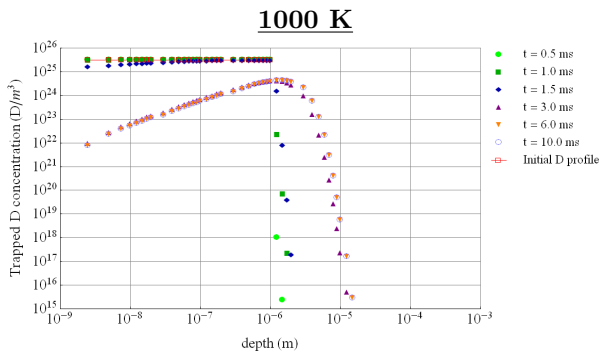
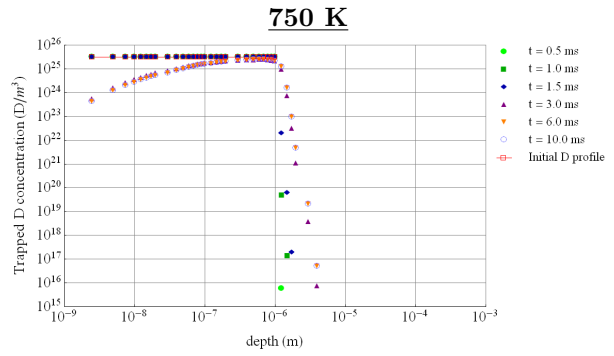
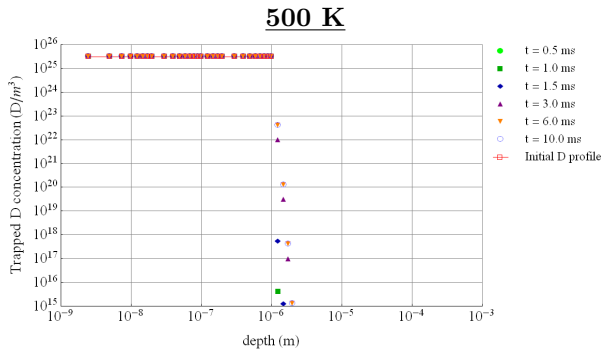
The experimental work should initially focus on achieving an absolute calibration of the LID-QMS system at the TEAC. In order to perform an absolute calibration, a tungsten sample with a well-known, homogeneous D content should be exposed to several LID shots. The ‘new’ D concentration of the sample should then be determined by TDS and compared to the retrieved LID signals. The same experiment should be repeated multiple times in order to obtain some certainty regarding the results. Also, some laser characteristics still require further specification. The laser energy losses of Section 4.3 should be determined by using a laser joulemeter. A CCD chip can further be used to determine the laser irradiated area of the laser pulse. The CCD chip should be installed at the same distance to the lens as the samples. The intensity distribution as obtained from the CCD chip should uncover any flaws in the laser pulse.

If these steps have been achieved, several experiments can be initialized. One of these experiments could be to determine the total desorption as a function of maximum surface temperature, as was already done in the LID analysis of TMAP7. Another proposed experiment is to research the D concentration of the middle spot of a plasma-exposed target as a function of plasma-exposure time.

## References

- [1] J. Ongena and G. Van Oost, *Trans. of Fus. Sci. and Tech.* 57, 3-15 (2010);
- [2] A. Huber et al., *Fusion Engineering and Design* 86, 1336-1340 (2011);
- [3] J. Roth et al., *Journal of Nuclear Materials* 390-391, 1-9 (2009);
- [4] B. Schweer et al., *Journal of Nuclear Materials* 390-391, 576-580 (2009);
- [5] J.P. Van Dorsselaere et al., *Fus. Eng. and Des.* 84, 1905-1911 (2009);
- [6] B. Schweer et al., *Journal of Nuclear Materials* 363-365, 1375-1379 (2007);
- [7] F. Irrek. *Entwicklung einer In-situ-Meßmethode zur Bestimmung des Wasserstoffgehalts amorpher Kohlenwasserstoffschichten in Fusionsanlagen.* Dissertation, FZ Jülich-Zentralbibliothek Nr. 4279, 2008;
- [8] M. Zlobinski. *Laserinduzierte Desorption an plasmaerzeugten Wandbeschichtungen.* Diploma work, University of Düsseldorf, 2009;
- [9] M. Zlobinski. et al., *Fusion Engineering and Design* 86, 1332-1335 (2011);
- [10] J. Rapp et al., *Fusion Engineering and Design* 85, 1455-1459 (2010);
- [11] H.J.N. van Eck et al., *Appl. Phys. Lett.* 101, 224107 (2012);
- [12] M. Poon et al., *Journal of Nuclear Materials* 374, 390-402 (2008);
- [13] B. Schweer et al., 36th EPS Conference on Plasma Phys., 2009, P-1.188;
- [14] B.J. Hensen. *Effect of transient heat loads on plasma-exposed tungsten surfaces.* Internship report, University of Delft, 2012;
- [15] T.W. Hansch et al., *Sci. Am.* March 1979, 94-110 (1979);
- [16] G.R. Longhurst. *TMAP7: Tritium Migration Analysis Program, User Manual.* Idaho National Laboratory, INEEL/EXT-04-02352, 2008;
- [17] J. Ambrosek and G.R. Longhurst. *Verification and Validation of TMAP7.* Idaho National Laboratory, INEEL/EXT-04-01657, 2008;
- [18] G.M. Wright et al., *Journal of Nuclear Materials* 415, S636-S640 (2011);
- [19] M. Poon. *Deuterium trapping in tungsten.* Thesis, University of Toronto, 2004;
- [20] *IDL Tutorial: Programming in IDL.* ITT Visual Information Solutions, 2008.

# A TMAP7: Trapped D Profile



## B TMAP7: Mobile D Profile

